

Cite this: *J. Mater. Chem. C*, 2022, 10, 3593

Solution-processable phenothiazine and phenoxazine substituted fluorene cored nanotextured hole transporting materials for achieving high-efficiency OLEDs†

Mangey Ram Nagar,^a Abhijeet Choudhury,^a Daiva Tavgeniene,^b Raminta Beresneviute,^b Dovydas Blazelevicius,^b Vyngintas Jankauskas,^c Krishan Kumar,^d Subrata Banik,^e Subrata Ghosh,^{id} Saulius Grigalevicius^{id}*^b and Jwo-Huei Jou^{id}*^a

Solution-processable hole-transporting materials (HTMs) are key functional materials for high-throughput and inexpensive fabrication of high-efficiency organic light-emitting diodes (OLEDs). Herein, we have successfully synthesized a novel series of phenothiazine and phenoxazine substituted fluorene core-based HTMs, *i.e.* 10-hexyl-3-[2,7-di(naphthalen-1-yl)-fluoren-9-ylmethylene]phenoxazine **DNFPhe**, 10-hexyl-3-[2,7-di(4-(diphenylamino)-phenyl)fluoren-9-ylmethylene]phenoxazine **DDPPFPhe**, 10-hexyl-3-[2,7-di(4-fluorophenyl)-fluoren-9-ylmethylene]phenoxazine **DFPPFPhe**, 10-hexyl-3-(2,7-diphenylfluoren-9-ylmethylene)phenoxazine **DPPFPhe**, 10-hexyl-3-[2,7-di(4-(diphenylamino)phenyl)fluoren-9-ylmethylene]phenothiazine **DDPPFPPh**, and 10-hexyl-3-[2,7-di(naphthalen-1-yl)fluoren-9-ylmethylene]phenothiazine **DNFPPh**, and incorporated them in solution-processed phosphorescent and thermally activated delayed fluorescence (TADF) OLEDs. The synthesized HTMs exhibit superior solubility in organic solvents and display nanotextured surface morphologies. These HTMs possess high hole-mobilities as compared to a conventional HTM, *N,N'*-bis(naphthalen-1-yl)-*N,N'*-bis(phenyl)-benzidine (**NPB**). By incorporating a phosphorescent bis(4-phenylthieno[3,2-*c*]pyridinato-*N,C2'*) (acetylacetonate) iridium(III) (**PO-01**) yellow emitter, we demonstrate an improvement in maximum power efficacy (PE_{\max}) from 41.6 to 45.4 lm W⁻¹, current efficacy from 39.8 to 50.6 cd A⁻¹, external-quantum efficiency (EQE_{\max}) from 12.9 to 19.6%, maximum brightness (L_{\max}) from 15 200 to 19 400 cd m⁻², and a lifetime (LT_{50}) from 151 to 465 h at 1000 cd m⁻² initial luminance of a phosphorescent OLED by substituting the conventional HTM, **NPB**, with **DDPPFPPh**. Additionally, the 2,4,5,6-tetra(9*H*-carbazol-9-yl)isophthalonitrile (**4CzIPN**) green TADF emitter-based OLED displays the enhancement in PE_{\max} from 42.5 to 69.1 lm W⁻¹, CE_{\max} from 54.1 to 78.0 cd A⁻¹, EQE_{\max} from 20.1 to 27.2%, L_{\max} from 12 900 to 44 200 cd m⁻² and LT_{50} from 195 to 590 h at an initial brightness of 1000 cd m⁻² by replacing **NPB** with **DDPPFPPh**. Based on these findings, the reported solution-processable HTMs appear to be promising candidates for high-efficiency OLEDs.

Received 2nd November 2021,
Accepted 30th January 2022

DOI: 10.1039/d1tc05237c

rsc.li/materials-c

1. Introduction

Organic light-emitting diode (OLED) technology has become the backbone of display technology after undergoing rapid

adoption by major technological companies such as Apple, Samsung and Google.^{1–5} It is expected to be the mainstay technology of the display industry for at least the next decade.^{6–10} OLED technology is also increasing its presence in the lighting industry with applications in a diverse field from lighting panels to being used as high-end automotive taillights.^{11–14} However, the devices are fabricated using a thermal evaporation process which makes the process overall quite expensive with numerous disadvantages such as high-power consumption, restrictions in scalability, decreased throughput, high rate of material consumption, complex color patterning process and non-uniform film deposition for large area fabrication while maintaining an enhanced resolution in pixels.^{15–17} This also delays the further commercialization and

^a Department of Materials Science and Engineering, National Tsing Hua University, Hsinchu, 30013, Taiwan. E-mail: jjou@mx.nthu.edu.tw

^b Department of Polymer Chemistry and Technology, Kaunas University of Technology, Radvilenu Plentas 19, LT50254, Kaunas, Lithuania. E-mail: saulius.grigalevicius@ktu.lt

^c Vilnius Univ, Inst Chem Phys, LT10257, Vilnius, Lithuania

^d School of Basic Sciences, Indian Institute of Technology Mandi, India

^e Department of Chemistry, School of Chemical and Biotechnology, SASTRA Deemed University, Thanjavur 613401, Tamil Nadu, India

† Electronic supplementary information (ESI) available. See DOI: 10.1039/d1tc05237c

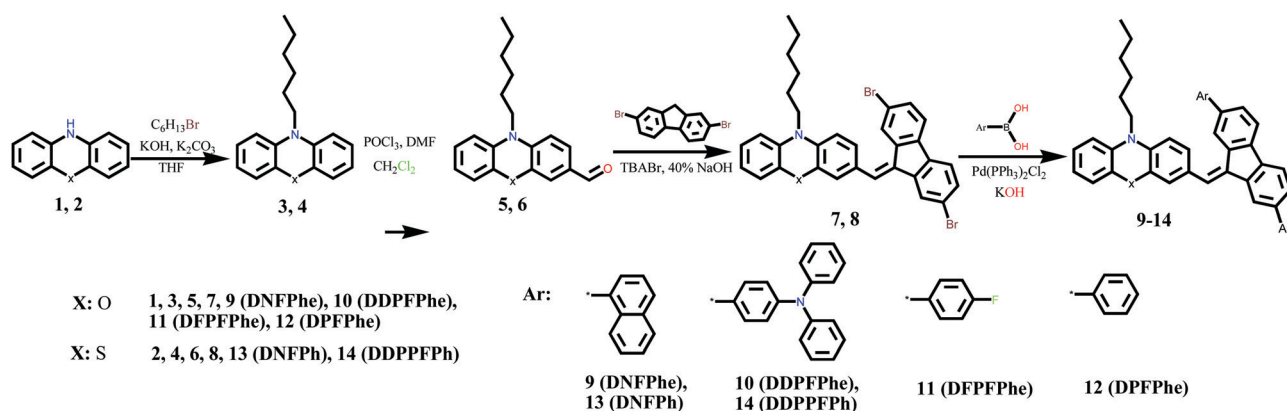
adoption of the OLED technology due to the high costs involved. The adoption of solution-processable fabrication processes can mitigate this problem by providing an inexpensive pathway for the fabrication of large-area efficient devices with a much higher utilization rate of materials.^{18,19} Incorporation of superior organic hole transport materials (HTMs) is a significant avenue that can allow the fabrication of high-efficiency OLED devices.²⁰ They play a crucial role in aiding stepwise charge transfer by decreasing the energy barriers thus allowing effective recombination in the emissive layer while decreasing recombination losses at the interfaces.^{21–25} Organic HTMs generally consist of small molecules or polymers which show a conducting nature. They exhibit superior hole mobility while being able to form morphologically stable films.^{16,26,27} The triplet energy of the HTMs should be higher than the emitters for effective confinement of triplet excitons as well as to ensure a low energy barrier to ensure the passage of holes from the anode to the emissive layer.²⁸ Some other properties include a high glass transition temperature and low tendency for crystallization even at high temperatures.^{29,30}

Considering the above-mentioned properties, researchers have synthesized and incorporated arylamine-based, amine-based, carbazole-based and carbazole–arylamine hybrid-based HTMs. *N,N'*-Diphenyl-*N,N'*-bis(1-naphthyl)-(1,1'-biphenyl)-4,4' diamine (NPB) and 1,1-bis((di-*t*-tolylamino)phenyl)-cyclohexane (TAPC) are some of the majorly used HTMs belonging to the arylamine class.^{30,31} Some major amine-based HTMs commercially used are 4,4',4''-tris[(3-methylphenyl)phenylamino]triphenylamine (MTDATA), 4,4',4''-tris(*N*-3-methylphenyl-*N*-phenylamino)triphenylamine (*m*-MTDATA) and 4,4',4''-tris(diphenylamino)triphenylamine (TDATA) generally known for their high glass transition temperature.^{32,33} The carbazole–arylamine hybrid-based HTMs consist of 1,3-bis(*N*-carbazolyl)benzene (mCP), 3,6-bis(4-vinylphenyl)-9-ethylcarbazole (VPEC) and 4,4',4''-tris(carbazol-9-yl)triphenylamine (TCTA).^{34–36} Although all these molecules have shown good device performance in the thermal evaporation process, some of their device performances have been poor in the solution process due to poor film formation, being morphologically less stable and due to crystallization of the film at room temperature.³⁷ The amine and carbazole-based HTM synthesis and purification process is difficult as well as expensive which limits its commercialisation potential.

Due to the relatively low intrinsic hole mobility shown by the films, they are required to be doped by p-type materials to enhance their mobility.^{38,39} Thus, there has been an increasing need to create a new class of HTMs with a cheaper synthesis process that can achieve a high-efficiency solution-processable device.

One of the strategies in designing a high-performance hole transport material involves the introduction of fluorene into the donor (D) and acceptor (A) units of these small molecules. This allows for the downshift of energy levels without having to forego the optical bandgap due to the electronegative nature of fluorene.^{40,41} The thin film morphology also shows improvement due to the enhancement of non-covalent interaction and intermolecular aggregation of H–F and C–F.⁴² The small size of the fluorine atoms leads to lower steric hindrance while allowing greater planarity to allow better charge transport.^{43,44} However, fluorination can contribute to low solubility in organic solvents and show increased aggregation in a thin-film state.^{45,46} This requires careful optimization of the degree of fluorination to achieve high-performance devices.

In this report, we have successfully synthesized a novel series of phenothiazine and phenoxazine substituted fluorene core-based HTMs. We have incorporated the above synthesized HTMs in phosphorescent bis(4-phenylthieno[3,2-*c*]pyridinato-*N,C2'*) (acetylacetonate) iridium(III) (**PO-01**) yellow emitter based devices where the best device showed an improvement in power (PE) from 31.3 to 41.4 lm W⁻¹, current efficacy (CE) from 35.0 to 48.2 cd A⁻¹ and external-quantum efficiency (EQE) of 11.3 from 18.7%, at 100 cd m⁻² when it was used in place of the conventional HTM NPB. We also fabricated 2,4,5,6-tetra(9*H*-carbazol-9-yl)isophthalonitrile (**4CzIPN**) green TADF emitter-based OLED devices with the best device displaying an enhancement in PE from 29.4 to 53.2 lm W⁻¹, CE from 48.4 to 71.6 cd A⁻¹, and EQE from 18.1 to 25.0%, at 100 cd m⁻². The synthesized HTMs show good solubility and nanotextured surface morphology. This allows the films to enhance the performance not only electrically by providing a cascaded charge transfer route but also optically by allowing an inner scattering medium for light extraction leading it to further contribute to the enhancement of external quantum efficiency.⁴⁷



Scheme 1 Synthesis of phenothiazine and phenoxazine substituted fluorene derivatives.

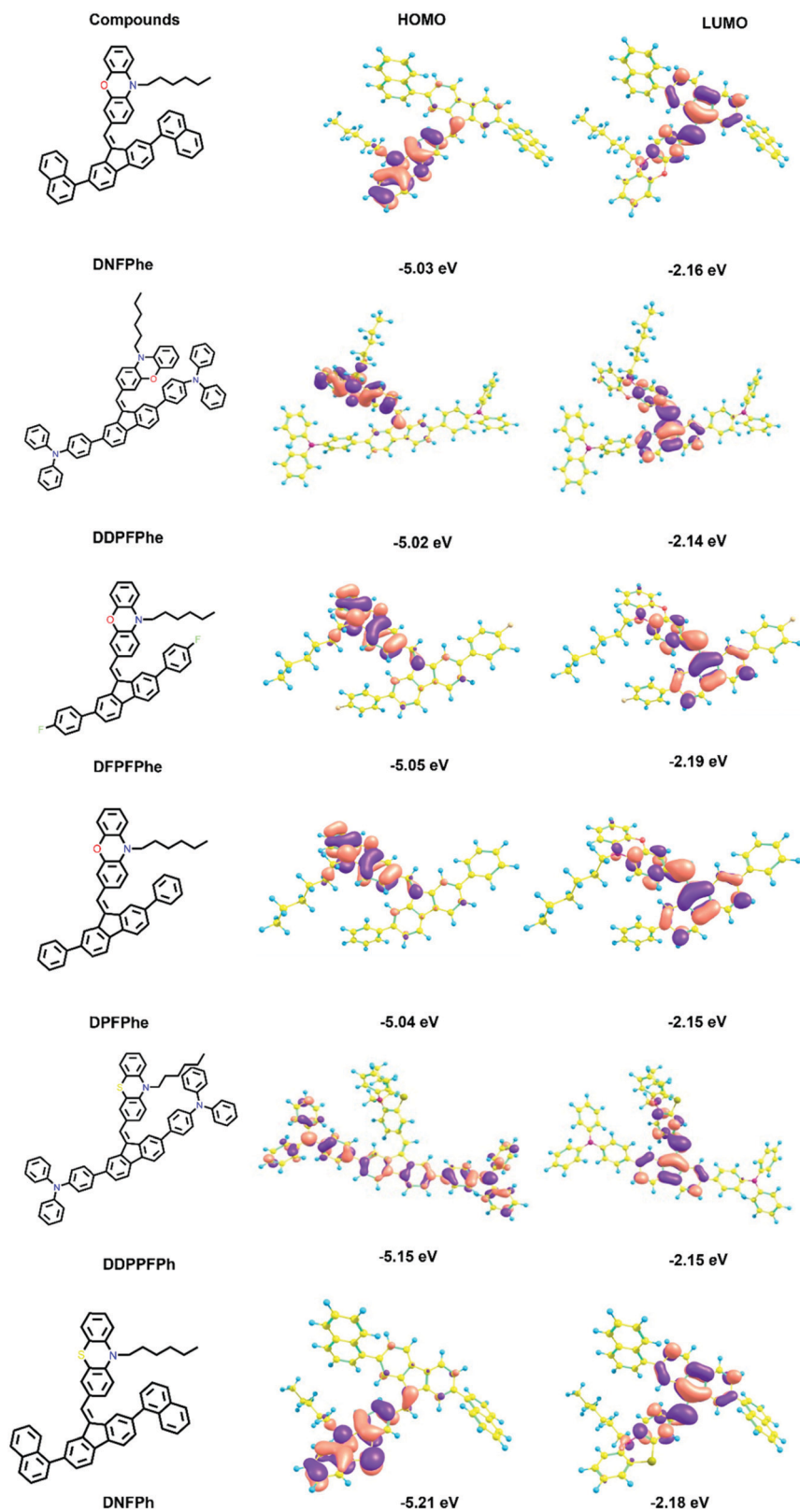


Fig. 1 Chemical structures and theoretically optimized molecular geometries of DNFPh, DDPFPh, DFPFPh, DPFPh, DDPPPh, and DNFPh.

2. Results and discussions

2.1. Synthesis

The synthesis of the diarylfluorene-based compound was carried out following the synthetic route as shown in Scheme 1. 10-Hexylphenoxazine (3) and 10-hexylphenothiazine (4) were prepared from 10*H*-phenoxazine (1) or 10*H*-phenothiazine (2), respectively, by alkylation reaction with 1-bromohexane under basic conditions. The alkylated products 3 and 4 were then converted into aldehydes: 3-formyl-10-hexylphenoxazine (5) and 3-formyl-10-hexylphenothiazine (6) by Vilsmeier formylation reaction. The key starting materials: 10-hexyl-3-(2,7-dibromofluoren-9-ylmethylene)phenoxazine (7) and 10-hexyl-3-(2,7-dibromofluoren-9-ylmethylene)phenothiazine (8) were then prepared by reactions of the aldehydes 5 and 6 with an excess of 2,7-dibromofluorene. Objective electroactive materials: 10-hexyl-3-(2,7-diarylfluoren-9-ylmethylene)phenoxazines (9–12) and 10-hexyl-3-(2,7-diarylfluoren-9-ylmethylene) phenothiazines (13–14) were finally synthesized from the dibromo-derivatives 7 or 8 using the Suzuki procedure by using, correspondingly, excess of naphthalene-1-boronic acid, 4(diphenylamino)phenylboronic acid, 4-fluorophenylboronic acid or phenylboronic acid. The newly synthesized derivatives were identified *via* mass spectrometry, FT-IR and NMR spectroscopy. The data were found to be in good agreement with the proposed structures.

2.2. Theoretical calculations

To establish the relationship between electronic structure, and the electrochemical and photophysical properties of the synthesized compounds, the ground state geometries were optimized using the hybrid functional B3LYP along with a 6-311G (d,p) basis set in Gaussian09 software.⁴⁸ All the calculations were carried out in solvent phase (THF) using a polarizable continuum model.⁴⁹ The spatial distributions of HOMOs and LUMOs of all the compounds are shown in Fig. 1. Due to the twist between phenoxazine (D) and fluorene (A) units, the highest occupied molecular orbital (HOMO) was mostly localised on the phenoxazine unit with very limited spread over the fluorene unit, as shown in Fig. 1. This confirms that the phenoxazine rings are not in the same plane with the fluorene

unit and thus these compounds must have limited π -conjugation along the molecular backbone. The separated HOMO and LUMO within the same molecule confirm that all the molecules possess donor–acceptor properties in their architecture. But the situation is different for DNFPhe in which the LUMO is located on the fluorene unit and HOMO is spread over the triphenylamine and fluorene unit. The shifting of HOMO from phenoxazine to triphenylamine (i.e. DNFPhe) may be due to the strong donor ability and extent of conjugation of the triphenylamine with the fluorene ring. The computational results are consistent with the experimental results (Table 1). Since the singlet and triplet energy levels are crucial factors for device performance, these energy levels are calculated using the time-dependent DFT (TD-DFT) with the same level of theoretical method using Tamm–Dancoff approximation (TDA) for the triplet states to avoid the triplet instability. The computed excitation energies are vertical, since the excited state geometries are not optimized. Although the optimized excited states ought to provide a better estimation for the transition energies, the vertical approximations enable us to calculate the oscillator strengths for the excitations directly. The calculated energy values of the singlet states (S1) for DNFPhe, DDPFPhe, DFPPFhe, DPFPh, DDPPFPh, and DNFPhe are 2.51, 2.52, 2.50, 2.52, 2.59 and 2.63, respectively and the energies of the triplet (T1) states are 1.97, 1.98, 1.97, 2.00, 2.25, and 2.11 eV for DNFPhe, DDPFPhe, DFPPFhe, DPFPh, DDPPFPh, and DNFPhe, respectively.

The T_1 values of DDPPFPh, and DNFPhe are higher than that of DNFPhe, DDPFPhe, DFPPFhe, and DPFPh. These high T_1 levels could suppress reversed exciton energy transfer from the guest to the host in the emitting layer and thus, enabled an efficient exciton capture in the emitting dopants. The theoretical UV-vis spectrum in the solvent phase is represented in Fig. S1–S6 (ESI[†]). The high-intensity peak in the theoretical UV-vis spectrum appears at 493, 491, 494, 491, 477 and 470 nm for DNFPhe, DDPFPhe, DFPPFhe, DPFPh, DDPPFPh, and DNFPhe respectively. These are attributed to the charge transfer phenomenon between donor (D) and acceptor (A) moieties.

Table 1 Photophysical, thermal, theoretical, and electrochemical characteristics of the novel phenothiazine and phenoxazine substituted fluorene core hole-transporting materials

Comp.	λ_{abs}^a (nm)	λ_{PL}^b (nm)	λ_{PL}^c (nm)	T_m^d (°C)	T_g^e (°C)	T_d^f (°C)	HOMO/LUMO ^g (–eV)	HOMO/LUMO ^h (–eV)	E_s/E_t^i (–eV)	E_s/E_t^j (–eV)	E_g^k (eV)	μ_h^l (cm ² V ^{–1} s ^{–1})
DNFPhe	404	527	548	—	91	357	5.03/2.17	5.32/2.27	2.51/1.97	2.67/2.59	3.07	4.9×10^{-3}
DDPFPhe	386	513	538	184	93	353	5.03/2.15	5.32/2.25	2.52/1.98	2.74/2.58	3.21	5.7×10^{-3}
DFPPFhe	402	517	557	158	64	382	5.06/2.20	5.38/2.30	2.50/1.97	2.72/2.57	3.08	4.5×10^{-3}
DPFPh	403	513	552	144	53	384	5.04/2.16	5.35/2.26	2.52/2.00	2.71/2.56	3.07	6.7×10^{-3}
DDPPFPh	337	515	537	231	107	391	5.16/2.16	5.84/2.16	2.59/2.25	2.70/2.69	3.68	5.7×10^{-3}
DNFPhe	367	503	540	—	93	373	5.21/2.19	5.57/2.19	2.63/2.10	2.67/2.66	3.38	8.1×10^{-3}

^a Absorbance peaks. ^b Photoluminescence (PL) spectra peak measured at room temperature. ^c PL spectra peak measured at 77 K. ^d Melting temperature. ^e Glass transition temperature. ^f Decomposition temperature. ^g HOMO and LUMO were calculated *via* DFT. ^h The redox potential obtained using a cyclic voltammetry (CV) technique gives HOMO and LUMO. The potential to semi-oxidation ($E_{1/2}^{\text{ox}}$) from $(E_{\text{p1}} + E_{\text{p2}})/2 - 0.48$ has been computed, where 0.48 is correctly estimated as the value of ferrocenium/ferrocene (Fc⁺/Fc) has been included in the internal standard. Then the energy from the HOMO = $-(E_{1/2}^{\text{ox}} + 4.8)$ was found. The LUMO energy level was calculated by removing the gap from the HOMO, $[E_{\text{LUMO}} = -E_{\text{HOMO}} + E_g]$. ⁱ Calculated triplet (E_t) and singlet (E_s) energy by DFT. ^j Measured triplet (E_t) and singlet (E_s) energy. ^k Measured optical band-gap (E_g) energy. ^l Measured hole-mobility (μ_h) with the time-of-flight technique.

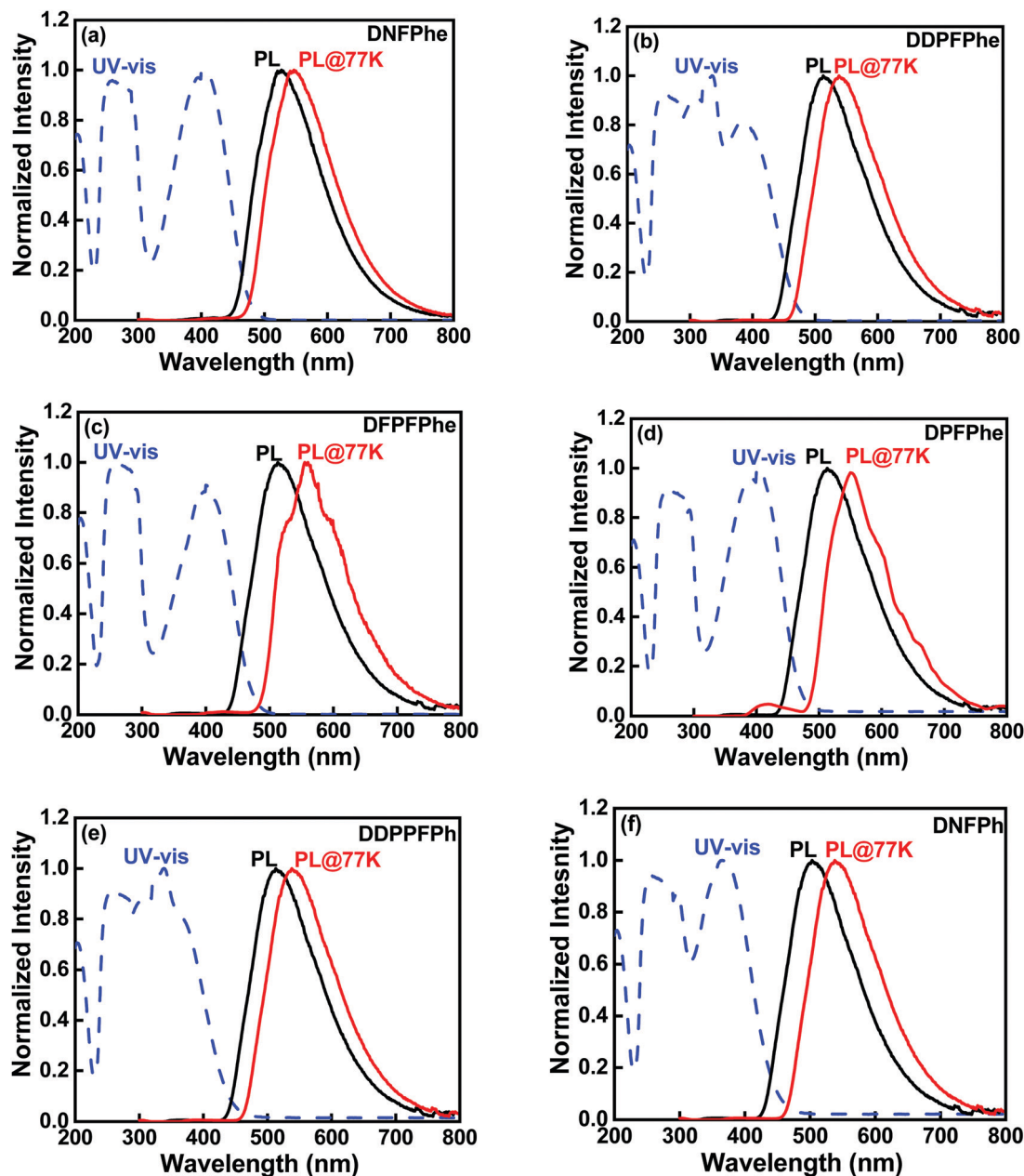


Fig. 2 Normalized ultraviolet-visible (UV-vis) absorption and photoluminescence (PL) spectra in tetrahydrofuran solution at room temperature, and phosphorescence (PL@77 K) spectra in tetrahydrofuran solution at 77 K for **DNFPh**, **DDPFPh**, **DFPFPh**, **DPFPh**, **DDPPFPh**, and **DNFPh**.

2.3. Photophysical and electrochemical properties

The ultraviolet-visible (UV-vis) spectra and photoluminescence spectra of the compounds **DNFPh**, **DDPFPh**, **DFPFPh**, **DPFPh**, **DDPPFPh**, and **DNFPh** were measured by dissolving these in tetrahydrofuran at room temperature, as shown in Fig. 2. We also measured same spectra in the solid state of newly synthesized HTMs, as shown in Fig. S7 (ESI[†]). It can be observed that the solid-state films of the newly synthesized HTMs displayed the same tendency in the UV/PL spectra as shown by the solution phase, although the difference is small. The optical band-gap energies were calculated from the edge of the absorption spectra, exhibiting values of 3.07, 3.21, 3.08,

3.07, 3.68, and 3.38 eV for the compounds **DNFPh**, **DDPFPh**, **DFPFPh**, **DPFPh**, **DDPPFPh**, and **DNFPh**, respectively. The triplet-energies were estimated from the first triplet peak of the low-temperature PL spectra, which was measured at 77 K in cryogenic medium (liquid nitrogen). The compounds **DDPPFPh** and **DNFPh** exhibited high triplet-energies of 2.69 and 2.66 eV, respectively, while the compounds **DNFPh**, **DDPFPh**, **DFPFPh**, and **DPFPh** displayed triplet-energies of 2.59, 2.58, 2.57, and 2.56 eV, respectively. All the photophysical properties are summarized in Table 1. The compounds **DDPPFPh** and **DNFPh** displayed higher triplet-energies as compared to the other compounds, **DNFPh**, **DDPFPh**, **DFPFPh**, and **DPFPh**,

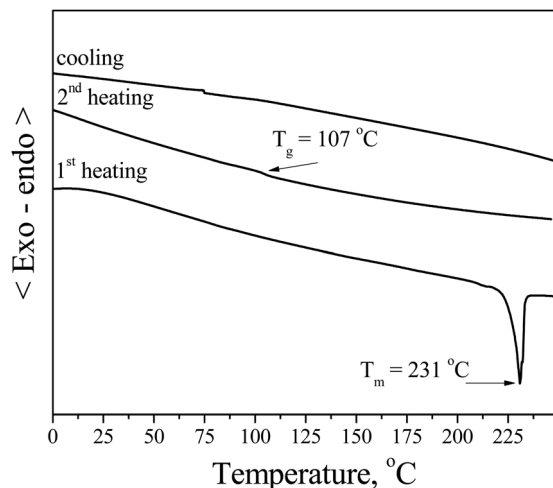


Fig. 3 DSC curves of compound DDPPFPhe. Heating rate: 10 °C min⁻¹.

which may be attributed to their extended conjugation in molecular structure, while the other compounds exhibited an interrupted conjugation long chain. As reported by Woon *et al.*, the triplet energy would decrease with the increase in effective conjugation length.⁵⁰ As shown in Fig. S8 (ESI[†]), the electrochemical properties of these phenothiazine and phenoxazine substituted fluorene cored HTMs, *i.e.* DNFPh, DDPPFPhe, DFPPPh, DPFPhe, DDPPFPhe, and DNFPh, were estimated by cyclic voltammetry (CV). The highest occupied molecular orbital (HOMO) energy levels of DNFPh, DDPPFPhe, DFPPPh, DPFPhe, DDPPFPhe, and DNFPh were calculated to be 5.32, 5.32, 5.38, 5.35, 5.84, and 5.57 eV respectively, using oxidation potential, while the lowest occupied molecular orbital (LUMO) energy-levels were estimated to be 2.27, 2.25, 2.30, 2.26, 2.16, and 2.19 eV for the compounds DNFPh, DDPPFPhe, DFPPPh, DPFPhe, DDPPFPhe, and DNFPh, respectively, from the HOMO energy-levels and optical bandgap energies, which were calculated from the absorption spectra, as shown in Table 1.

2.4. Thermal and morphological properties

The behaviour under heating of the synthesized objective materials DNFPh–DNFPh was studied by DSC and TGA under a nitrogen atmosphere. The results are presented in Table 1. It was established that the derivatives demonstrate very high thermal stability. The temperatures of 5% weight loss for the materials corresponded to 357 °C for DNFPh, 353 °C for DDPPFPhe, 382 °C for DFPPPh, 384 °C for DPFPhe, 391 °C for DDPPFPhe and 373 °C for DNFPh as confirmed by TGA with a heating rate of 10 °C min⁻¹. The compounds DNFPh and DDPPFPhe were obtained after synthesis as amorphous materials with high glass transition temperatures as confirmed by DSC. When samples of the materials DNFPh and DDPPFPhe were heated during the DSC experiment, glass transitions were observed correspondingly at 91 °C for DNFPh and at 107 °C for DDPPFPhe, and no peaks due to crystallization and melting appeared during the further heating and cooling scans. Other derivatives (DDPPFPhe, DFPPPh, DPFPhe and DNFPh) were obtained as crystalline materials after the synthesis as confirmed by DSC, however, they could be converted to amorphous materials by cooling their melted samples. The values of glass transition temperatures (*T_g*) of the derivatives are summarized in Table 1.

DSC thermo-grams of the compound DDPPFPhe are shown in Fig. 3 as an example. When the crystalline sample of DDPPFPhe was heated, the endothermic peak due to the melting of the crystals was observed at 231 °C. When the melted sample was cooled down, it formed an amorphous material. During the second heating of the sample, only the glass transition was observed at 107 °C and on further heating, no peaks due to crystallization and melting appeared. The high thermal stabilities and rather high glass transition temperatures of the objective materials demonstrate their greater potential for the preparation of thin, thermally stable amorphous layers for OLED devices.⁵¹

The surface morphology of the active layers deposited on HTMs plays a crucial role in deciding the performance of

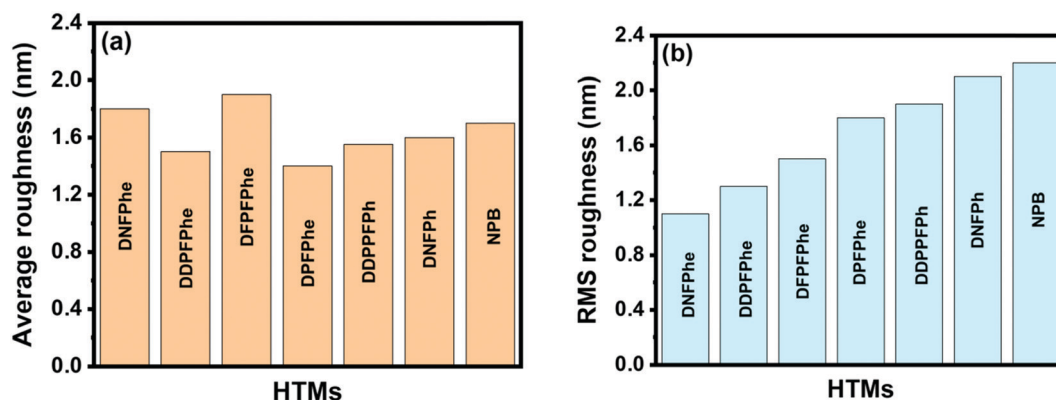


Fig. 4 (a) Average roughness and (b) root mean square (RMS) roughness of the novel HTM thin-films, *i.e.* DNFPh, DDPPFPhe, DFPPPh, DPFPhe, DDPPFPhe, DNFPh, and NPB, prepared on PEDOT:PSS thin-film. It can be observed that all HTMs show a lower mean average roughness as compared to NPB. Phenothiazine based HTMs display a lower average roughness, while phenoxazine based HTMs show a higher average roughness as compared to NPB.⁵²

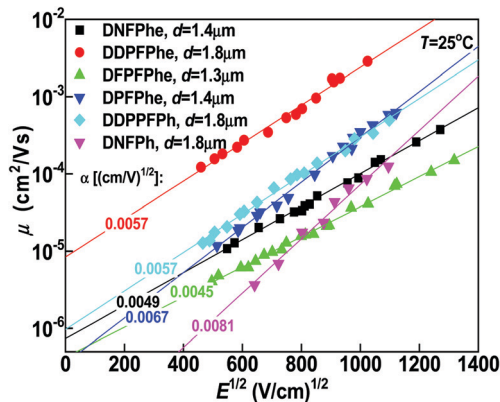


Fig. 5 Electric field dependencies of the hole drift mobilities (μ) in the charge-transport layers of the hole transporting materials DNFPhe–DNFPPh.

high-efficiency OLEDs. The surface morphologies of the spin-casted thin films of the HTMs were observed using atomic force microscopy (AFM) by scanning a $10 \times 10 \mu\text{m}^2$ surface area, as

shown in Fig. S9 (ESI[†]). The resultant root mean square surface roughness values of the organic materials DNFPhe, DDPFPhe, DFPFPhe, DPFPhe, DDPFPPh, DNFPh, and NPB are 1.1, 1.3, 1.5, 1.8, 1.9, 2.1, and 2.2 nm, respectively, as shown in Fig. 4. All the spin-casted thin films of the HTMs display smooth surface topographies without any defects and crystallization. As shown in Fig. S10 (ESI[†]), phenoxazine and phenothiazine-based HTMs exhibit nanotextures on the surfaces, while NPB displays planer surfaces. The nanotexture surface of these HTMs plays a role of inner scattering medium for extracting light-out from the device to further increase the external quantum efficiency.

2.5. Charge carrier transport properties

The hole-mobility (μ_h) of the newly synthesized organic materials DNFPhe, DDPFPhe, DFPFPhe, DPFPhe, DDPFPPh, and DNFPh was measured using the xerographic time of flight technique (XTOF).⁵³ The μ_h was calculated by using the formula of $\mu_h = d^2/(V \cdot t_T)$, where d represents the layer thickness of the materials, V is the applied voltage, and t_T is the carrier transport time. Fig. 5 displays the μ_h measured for the fluorene

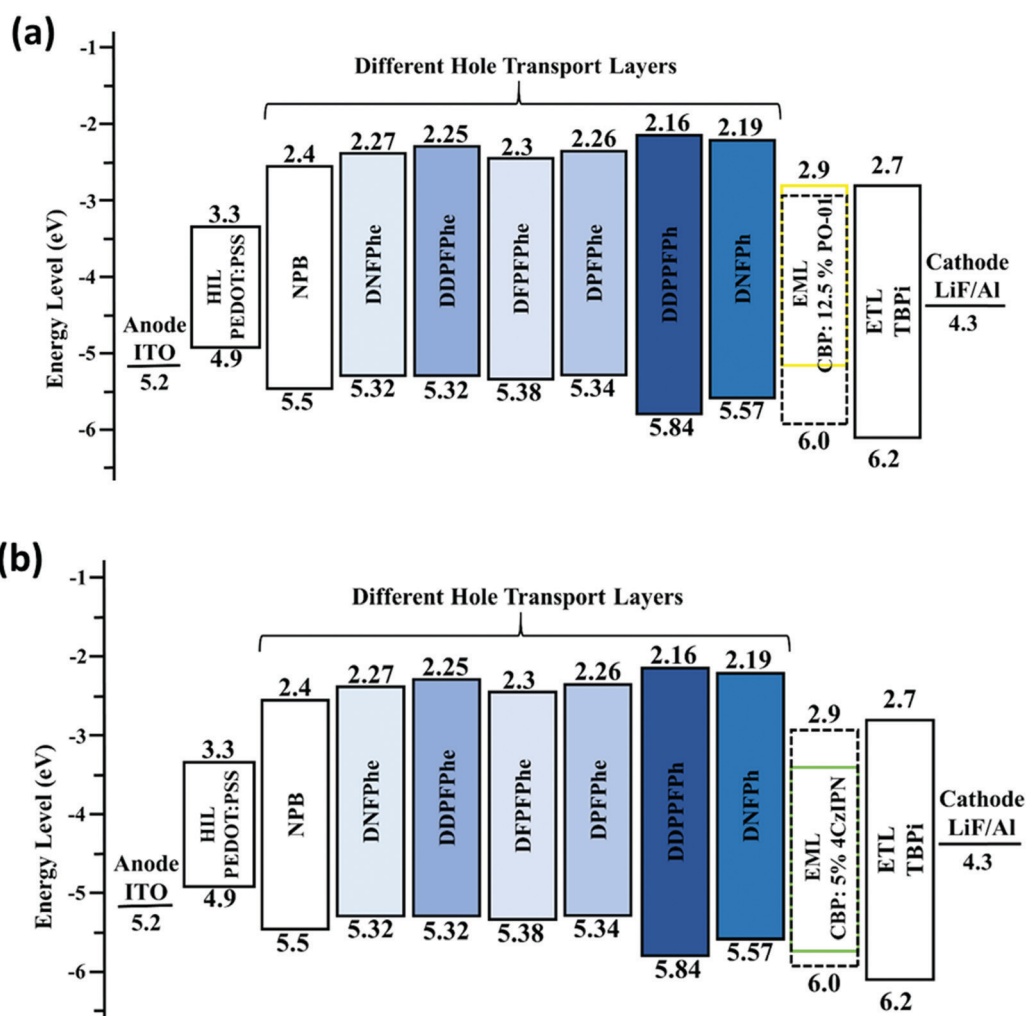


Fig. 6 The energy-level diagram of the solution-processed (a) yellow phosphorescent and (b) green TADF OLED devices comprising the spin-coated thin-films of seven different HTMs: NPB, DNFPhe, DDPFPhe, DFPFPhe, DPFPhe, DDPFPPh, and DNFPh.

cored based HTMs, which has shown μ_h as a function of the square root of electric field ($E^{1/2}$). The transient photocurrent curves are shown in Fig. S11 (ESI†). The μ_h of organic materials **DNFPhe**, **DDPPFphe**, **DFPFphe**, **DPPFphe**, **DDPPFPh**, and **DNFPPh** are 4.9×10^{-3} , 5.7×10^{-3} , 4.5×10^{-3} , 6.7×10^{-3} , 5.7×10^{-3} , and $8.1 \times 10^{-3} \text{ cm}^2 \text{ V}^{-1} \text{ s}^{-1}$, respectively, which are shown in Table 1.

2.6. Electroluminescent properties

To investigate the hole-injection and transport properties of the newly synthesized HTMs, we have fabricated a device using a conventional phosphorescent yellow emitter with the following

configuration: ITO (125 nm)/PEDOT:PSS (35 nm)/HTMs/CBP:12.5 wt% **PO-01**(20 nm)/TPBi (45 nm)/Al (100 nm) and also a device with a conventional TADF green emitter with the following device configuration ITO (125 nm)/PEDOT:PSS (35 nm)/HTMs/CBP:5 wt% **4CzIPN** (20 nm)/TPBi (45 nm)/Al (100 nm). The schematic energy-level diagrams of the studied yellow phosphorescent and green TADF OLED devices are shown in Fig. 6. The well-known phosphorescent yellow and TADF green emitters, **PO-01** and **4CzIPN**, respectively, were selected as the emissive materials due to their suitable HOMO–LUMO levels, band gap energies, and triplet energies, as compared with the CBP host. Control devices were also

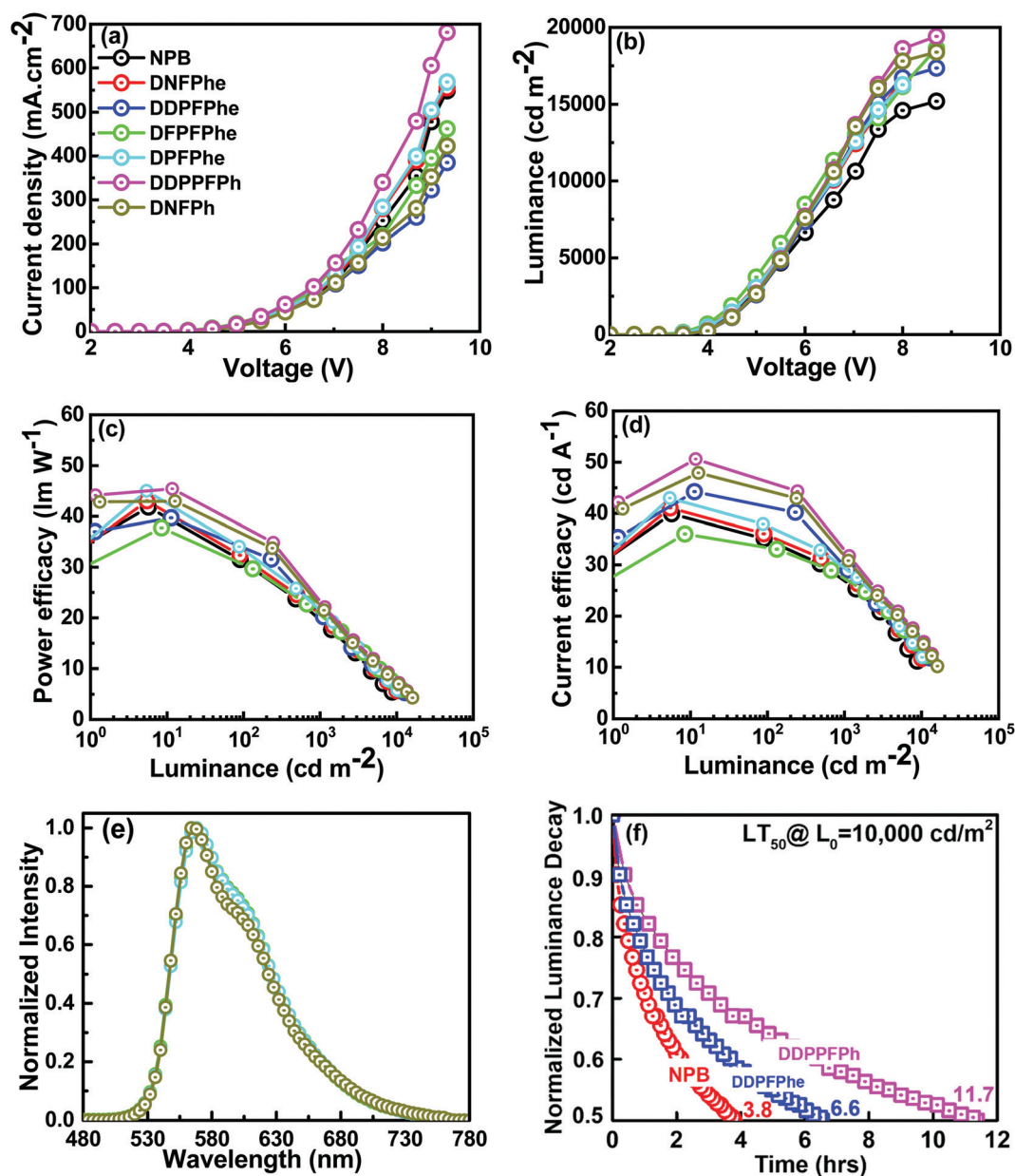


Fig. 7 Effects of different HTMs on the (a) current density vs. voltage, (b) luminance vs. voltage, (c) power efficacy vs. luminance, (d) current efficacy vs. luminance, (e) EL spectra of the phosphorescent OLED devices, and (f) normalized luminance vs. an operational lifetime of solution-processed yellow phosphorescent OLEDs having HTLs of NPB, DDPPFphe or DDPPFPh.

Table 2 Summarized electroluminescent properties of yellow phosphorescent OLEDs with different hole-transporting materials

HTLs	Operation voltage (V)			EQE (%)	CIE @100 cd m ⁻²	I _{max} (cd m ⁻²)
	@ 100 cd m ⁻² /1000 cd m ⁻² /10 000 cd m ⁻² /maximum values	Power efficacy (lm W ⁻¹)	Current efficacy (cd A ⁻¹)			
NPB	3.5/4.3/6.8/3.0	31.3/20.4/4.6/41.6	35.0/27.5/9.9/39.8	11.3/8.7/3.1/12.9	(0.52, 0.48)	15 202
TAPC	3.5/4.3/7.2/3.0	31.3/10.3/7.9/35.3	34.8/13.1/8.8/33.7	12.5/9.5/2.7/12.5	(0.52, 0.48)	10700
α-NPD	3.6/4.4/7.1/3	25.5/15.6/3.2/34.2	28.8/21.9/7.1/32.9	9.3/6.9/2.2/10.7	(0.52, 0.48)	12506
DNFPhe	3.5/4.3/6.5/3.0	32.2/21.4/5.7/42.8	35.9/28.8/11.7/41.0	11.7/9.1/3.6/13.3	(0.52, 0.48)	16 632
DDPPPh	3.7/4.4/6.5/3.5	36.4/21.6/6.8/39.7	42.6/30.3/14.0/44.2	16.5/11.6/5.2/17.2	(0.51, 0.48)	17 345
DFPPPh	3.4/4.1/6.2/3.0	31.8/21.2/6.8/37.2	33.8/27.8/13.5/35.8	13.1/10.6/5.0/13.9	(0.52, 0.48)	18 627
DPFPhe	3.5/4.3/6.5/3.0	33.8/22.3/5.9/44.8	37.8/30/12.1/42.9	12.3/9.5/3.7/13.9	(0.52, 0.48)	16 258
DDPPPh	3.7/4.4/6.4/3.5	41.4/24.3/7.7/45.4	48.2/33.8/15.6/50.6	18.7/12.9/5.8/19.6	(0.51, 0.48)	19 409
DNFPhe	3.7/4.4/6.4/3.5	39.4/23.2/7.4/43.0	46/32.5/15.0/47.9	17.8/12.4/5.6/18.6	(0.51, 0.48)	18 382

fabricated with the most widely used commercial HTMs NPB and α-NPD that have the same device structure for comparing the attained results. The positive charge carriers enter into the device from the anode, injecting by PEDOT:PSS HOMO and transfer through the HOMO level of HTMs. At the same time, negative charge carriers inject into the device from the cathode injecting by LiF and transfer through the LUMO levels of TPBi. After reaching into the emissive layer, these charge carriers generate excitons and recombine in the emissive zone. Effective LUMO levels of the HTMs help to block the electron into the emissive layer, providing enhancement in performance. The fabrication process of yellow phosphorescent OLEDs includes the spin-coating of a solution of PEDOT:PSS on pre-cleaned ITO to form a hole-injection layer and spin-coating of the different hole-transporting materials solution to deposit the hole-transport layer, as shown in Fig. 6(a). This was followed by deposition of a premixed host CBP and phosphorescent emitter **PO-01** to form a phosphorescent emissive layer *via* solution processing followed by a gradual thermal annealing process. Formerly, the deposition of the electron-transporting layer TPBi, the electron-injection layer LiF and the cathode Al was carried out by thermal-evaporation in a thermal evaporator with a base vacuum pressure of less than 4×10^{-6} Torr. For comparative analysis, we also fabricated a control device with the conventional HTL of TAPC. As shown in Fig. 6(b), the green TADF OLED also contains PEDOT:PSS as the HIL, phenothiazine and phenoxazine substituted fluorene cored materials as the HTL and a green TADF emissive layer prepared by mixing CBP with **4CzIPN**. Finally, the electron-transport layer, electron injection layer and cathode were formed by thermal evaporation of TPBi, LiF and Al, respectively.

2.6.1. Phosphorescent OLED. The electroluminescence properties of yellow phosphorescent OLED are shown in Fig. 7 and their corresponding values are summarized in Table 2. The current density–voltage curves of different HTM based yellow phosphorescent OLEDs are presented in Fig. 7(a). We observed that the device with phenothiazine and phenoxazine substituted fluorene cored materials displays a higher current density as compared with NPB based devices. A comparable trend is observed in the luminance–voltage characteristics of these material-based yellow devices, as shown in Fig. 7(b). All six material-based OLED devices display higher power efficacies as compared to the conventional NPB based

HTL, as displayed in Fig. 7(c). All the devices with newly synthesized HTMs display the same trend in current efficacy–voltage curves, as demonstrated in Fig. 7(d).

The control OLED device with HTM **NPB** displays a PE, CE and EQE of 31.3 lm W⁻¹, 35.0 cd A⁻¹ and 11.3%, respectively, at 100 cd m⁻² along with a maximum brightness of 15 200 cd m⁻², respectively. In addition, the phenothiazine substituted fluorene cored HTM **DDPPPh** and **DNFPhe** based yellow phosphorescent OLED devices exhibit a PE of 41.4 and 39.4 lm W⁻¹ at the same brightness, which is nearly 32.3 and 25.9% higher than that of the conventional HTM, NPB, based device. Additionally, these material-based devices exhibit a brightness of 19 400 and 18 300 cd m⁻², respectively, which is 27.6 and 20.4%, respectively, higher than those of the conventional HTM **NPB** based device. At a brightness of 1000 cd m⁻², the PE, CE and EQE of the phenothiazine substituted fluorene cored HTM **DDPPPh** based yellow phosphorescent OLED device are noticeably enhanced from 20.4 lm W⁻¹, 27.5 cd A⁻¹ and 8.7% to 24.3 lm W⁻¹, 33.8 cd A⁻¹ and 9.5%, respectively, as shown in Fig. 7.

In addition, the phenoxazine HTM **DNFPhe**, **DFPPPh**, and **DPFPhe** based OLED devices display a PE_{max} of 42.8 lm W⁻¹ (CE_{max} of 41.0 cd A⁻¹ and EQE_{max} of 13.3%), PE_{max} of 37.2 lm W⁻¹ (CE_{max} of 35.8 cd A⁻¹ and EQE_{max} of 13.9%), and PE_{max} of 44.8 lm W⁻¹ (CE_{max} of 42.9 cd A⁻¹ and EQE_{max} of 13.9%), respectively, which are 3% (17.1 and 3.1%), 18.8% (2.3 and 7.8%) and 43.1% (22.6 and 7.8%) higher than the **NPB** based device. Moreover, these material-containing devices showed the brightness of 16 600, 18 600, and 16 200 cd m⁻². The higher performance of the phenoxazine and phenothiazine based devices is due to the following factors: (i) effective electron and exciton confinement within the emissive layer due to their shallower LUMO energy levels, particularly at high brightness or voltages, (ii) smooth surface morphologies of phenoxazine and phenothiazine based materials assisting in preventing any undesirable current-leakage during device measurement, (iii) comparatively high hole mobilities, (iv) perfect energy-level alignment of host and guest facilitating efficient hole-injection into the emissive layer, and (v) efficient high-triplet energies. The OLED devices with different newly synthesized HTMs display an EL emission spectra peak at 565 nm, as shown in Fig. 7(e). The operational lifetime of (LT₅₀) showing when the luminance drops to half of the primary luminance (L₀), of the

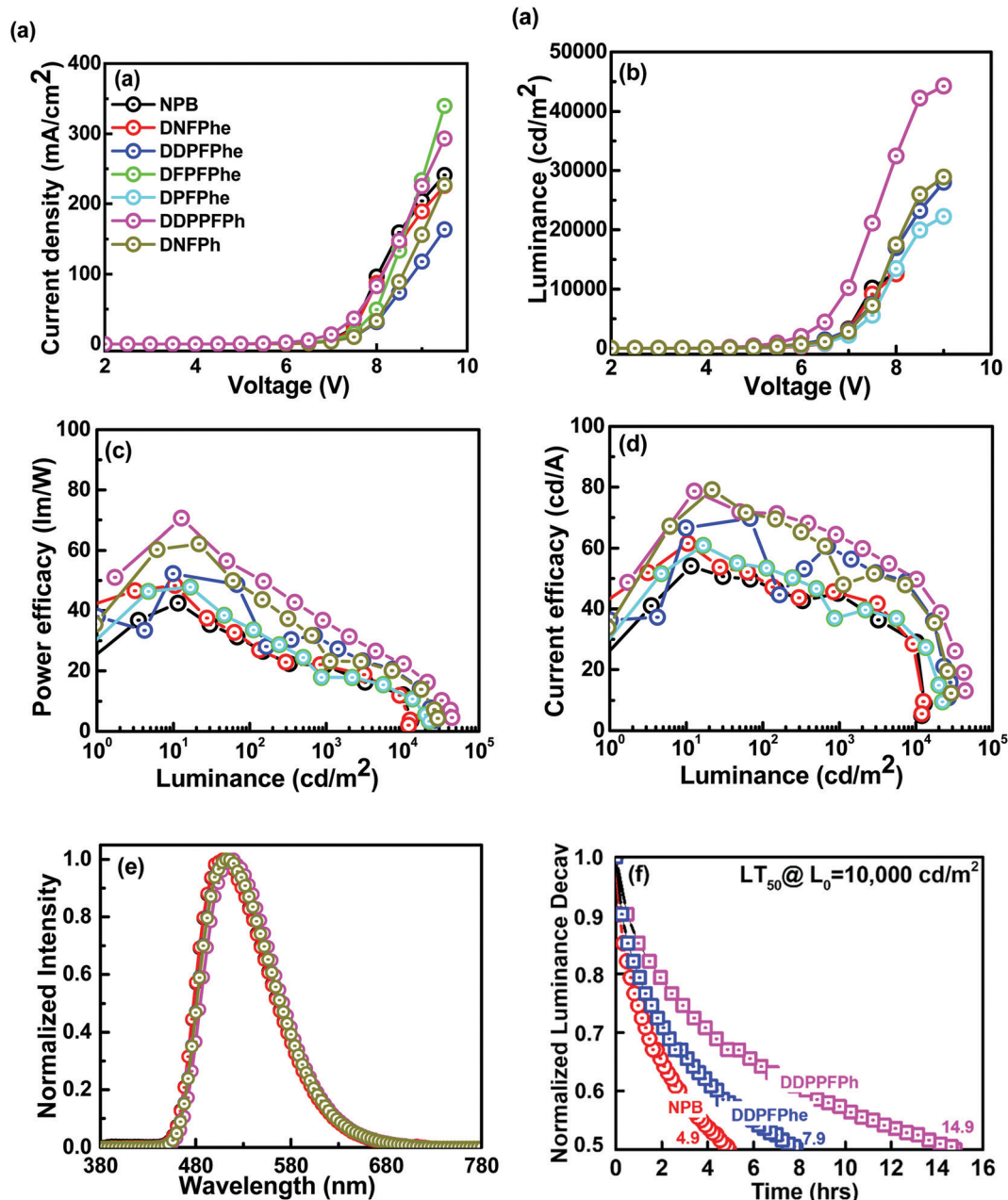


Fig. 8 Effects of different HTMs on the (a) current density vs. voltage (b) luminance vs. voltage, (c) power efficacy vs. luminance, (d) current efficacy vs. luminance, (e) EL spectra of the phosphorescent OLED devices, and (f) normalized luminance vs. an operational lifetime of solution-processed green TADF OLEDs having HTLs, NPB, DDPFPhe and DDPPFPPh.

phosphorescent OLEDs, was controlled by operating the devices under a steady current with variable initial brightness at room temperature. The effects of HTMs namely **NPB**, **DDPFPhe** and **DDPPFPPh** on the device lifetime is shown in Fig. 7(f). The phenothiazine substituted fluorene cored HTM **DDPPFPPh** displays a lifetime of 11.7 h at the initial brightness of $10\,000\text{ cd m}^{-2}$, while the conventional HTM **NPB** based device shows a lifetime of 3.8 h at the same initial brightness. Moreover, the LT_{50} of the phenothiazine-based device, at the initial luminance of 1000 cd m^{-2} , can be generalized to 465 h, which is higher than that of a conventional HTM **NPB** based

device (151 h). Additionally, the phenoxazine based HTM **DDPFPhe** exhibits the LT_{50} lifetime of 262 h at an initial luminance of 1000 cd m^{-2} , which is also higher than that of conventional HTM, **NPB** based OLEDs. These superior lifetime values may be attributed to the higher thermal stability of the newly synthesized materials as compared to the typical HTM, **NPB**.

2.6.2. TADF OLED. The electroluminescent properties of typical carbazole based **4CzIPN** green TADF devices fabricated with newly synthesized HTMs are displayed in Fig. 8 and summarized in Table 3. Fig. 8(a–d) demonstrate the

Table 3 Summarized electroluminescent properties of green TADF OLEDs with different hole-transporting materials

HTLs	Operation voltage (V)			Power efficacy (lm W ⁻¹)			Current efficacy (cd A ⁻¹)							
	@ 100 cd m ⁻² /1000 cd m ⁻² /10 000 cd m ⁻² /maximum values						EQE (%)			CIE @100 cd m ⁻²			L _{max} (cd m ⁻²)	
NPB	5.2/6.5/7.5/4.0	29.4/21.7/12.3/42.5	48.4/45.0/29.2/54.1	18.1/17.0/11.6/20.1	(0.27, 0.55)	12 905								
TAPC	5.2/6.5/7.5/4.0	29.3/21.6/12.2/42.4	48.3/44.8/29.1/53.9	13.0/12.2/8.3/14.5	(0.27, 0.55)	12 865								
α-NPD	5.2/6.5/7.5/3.9	33.6/24.1/13.2/48.4	55.2/50.1/31.6/61.4	20.6/18.8/12.4/24.6	(0.26, 0.55)	13 805								
DNFPhe	5.3/6.5/7.6/4.0	29.8/21.8/9.9/48.3	49.6/45.4/23.9/61.6	18.5/17.0/9.3/22.9	(0.27, 0.55)	12 550								
DDPFPh	4.7/6.2/7.6/4.0	41.9/29.9/18.9/52.3	61.5/58.9/45.7/66.6	22.2/21.3/16.7/24.2	(0.28, 0.57)	28 015								
DFPFPh	4.9/6.5/7.8/4.0	34.4/17.6/12.7/47.5	53.5/37.1/31.4/60.6	16.8/11.7/10.0/19.1	(0.28, 0.57)	21 530								
DPFPh	4.9/6.5/7.8/4.0	34.5/17.8/12.8/47.8	53.8/37.2/31.5/60.9	25.2/17.5/15.0/28.6	(0.28, 0.57)	22 230								
DDPPFPh	4.2/5.5/7.0/3.6	53.2/36.3/22.5/69.1	71.6/64.0/50.0/78.0	25.0/22.4/17.6/27.2	(0.29, 0.58)	44 278								
DNFPPh	4.7/6.4/7.6/4.0	47/25.5/18.4/62.1	70.6/51.4/44.6/79.1	25.5/18.6/16.3/28.6	(0.28, 0.57)	28 899								

current–density–voltage, luminance–voltage, power efficacy–luminance, and current efficacy–luminance properties of green TADF OLEDs fabricated with different newly synthesized HTMs. The conventional NPB based control device exhibits a PE of 29.4 lm W⁻¹, CE of 48.4 cd A⁻¹, EQE of 18.1% at 100 cd m⁻² having a maximum brightness of 12 900 cd m⁻², while the phenothiazine derivative-based (**DDPPFPh**) device displays a PE of 53.2 lm W⁻¹, CE of 71.6 cd A⁻¹, and EQE of 25% at the same brightness with a maximum luminance of 44 300 cd m⁻², which are 80.9, 47.9, 38.1, and 243% higher as compared to the NPB based device. Moreover, the improvement in CE from 45.0 to 64.0 cd A⁻¹, PE from 21.7 to 36.3 lm W⁻¹, and EQE from 17.0 to 22.4% at 1000 cd m⁻² was noticed. As shown in Fig. 8, the **DDPFPh** incorporating device exhibits a PE_{max} of 52.3 lm W⁻¹, CE_{max} of 66.6 cd A⁻¹ and EQE_{max} of 24.2% having a L_{max} of 28 000 cd m⁻². The reason why the **DDPPFPh** based device displayed the highest efficiencies among all seven investigated HTMs may be attributed to the high hole-mobility, suitable HOMO and LUMO energy levels, and adequately high triplet-energy.

The phenothiazine substituted fluorene cored materials, **DDPPFPh** and **DNFPPh**, exhibited higher hole mobilities of 5.7×10^{-3} and 8.1×10^{-3} cm² V⁻¹ s⁻¹, which are much higher than those of the conventional HTM **NPB** counterpart. The **DDPPFPh** favours efficient hole-injection into the emissive layer and shows the improved brightness out of all devices. Moreover, the device architecture with **DDPPFPh** and **DNFPPh** displays energy-barriers of 0.94 and 0.67 eV for holes to inject from PEDOT:PSS and of -0.04 and 0.23 eV to the **4CzIPN** guest, respectively. Meanwhile, the **DFPFPh** based device has an energy barrier of 0.48 eV for holes to inject from PEDOT:PSS to HTM and 0.42 eV additional energy barriers for holes to enter from the HTM to guest **4CzIPN**. The improved performance may be attributed to higher hole-mobilities and reduced hole-injection barriers between the HIL and HTL as well as between the HTL and EML.^{54–56} The phenothiazine substituted fluorene cored materials displayed a higher performance as compared to phenoxazine substituted fluorene cored materials. The reason why the devices show performance enhancement is due to their higher triplet energy (E_T) values, having deep HOMO levels and high hole-mobilities, as shown in Table 1.⁵⁷ Furthermore, we observed that all the HTMs exhibit a higher E_T (2.56–2.69 eV) than that of CBP (2.55 eV). The newly synthesized

HTMs can successfully bind and confine the excitons inside the emissive zone and provide brighter emissions along with high efficiencies as compared with the available HTMs.^{57–59} We have shown the energy-transfer mechanism in Fig. S12 (ESI†). Fig. 8(e) shows the EL spectra of the TADF OLED devices that were composed at 1000 cd m⁻². We also observed that the devices become more stable with the incorporation of phenothiazine and phenoxazine substituted fluorene derivatives as novel HTMs. Fig. 8(f) displays the effect of newly synthesized HTMs on the TADF OLED device lifetime. The **DDPPFPh** based TADF OLED exhibits a lifetime of 14.9 h, while other HTMs **NPB** and **DDPFPh** display the lifetime of 4.9 and 7.9 h at an initial brightness of 10 000 cd m⁻², respectively. We also observed an extrapolated lifetime at 1000 cd m⁻² for these HTMs, **NPB**, **DDPFPh** and **DDPPFPh** based devices to be 195, 315, and 590 h, respectively. At 100 cd m⁻², these HTM, **NPB**, **DDPFPh** and **DDPPFPh** based TADF devices display 7765, 12 520, and 23 615 h, respectively. The thermal degradation temperature of the HTMs plays a major role in lifetime estimation, which may lead to higher LT₅₀ under electrical excitation.^{60–62} Hence, it is very important to measure the degradation mechanism of phenothiazine and phenoxazine substituted fluorene cored HTMs. As shown in Table S1 (ESI†), we also compared our results with previous reports and found that these materials showed better performance. Our results indicate that the lifetime of solution-processed phosphorescent and TADF OLEDs can be improved further by modifying the molecular structure of phenothiazine and phenoxazine substituted fluorene core-based HTMs. These materials will open a path toward the fabrication of high-efficiency and stable OLEDs for display and lighting applications.

3. Conclusion

To summarize, we have designed and synthesized a series of phenothiazine and phenoxazine substituted fluorene cored HTMs, **DNFPPh**, **DDPFPh**, **DFPFPh**, **DPFPh**, **DDPPFPh**, and **DNFPPh**, for high-efficiency phosphorescent and TADF OLED devices. These six organic HTMs displayed superior solution-processability in conventional organic solvents resulting in a smooth thin-film morphology, which possibly led to improved thermal stability. Moreover, these HTMs exhibited higher hole

mobilities as compared to the typical commercial counterpart NPB. The OLED devices with these HTMs displayed higher device efficiencies than that of the NPB based device. A yellow phosphorescent OLED device exhibited an enhancement of 31, 37.7, 65.5 and 208%, in PE_{\max} , CE_{\max} , EQE_{\max} , and lifetime, respectively, when the conventional NPB was replaced with **DDPPFPPh** as the HTL. The green TADF OLED displayed a PE_{\max} of 69.1 lm W^{-1} , a CE_{\max} of 78.0 cd A^{-1} , an EQE_{\max} of 27.2%, and a lifetime of 590 h showing an enhancement of 62.5, 44.2, 35.3, and 202%, respectively, as compared with the NPB based OLED. This enhancement in device performance is attributed to the smooth surface topography, the rational hole transporting ability, high triplet-energies, and effective electron-confinement which helps in generating more excitons in the emissive zone. The present phenothiazine substituted fluorene derivatives could be possible solution-processable amorphous HTMs for fabricating highly efficient OLED devices. These results are expected to open a path for the field experts to design and synthesize novel materials toward the realization of stable and highly efficient OLEDs for solid-state lighting and display applications.

4. Experimental

4.1. Synthesis details and spectral data

10*H*-Phenoxazine (1), 10*H*-phenothiazine (2), 1-bromohexane, 2,7-dibromofluorene, naphthalene-1-boronic acid, 4-(diphenylamino)phenylboronic acid, 4-fluorophenylboronic acid, phenylboronic acid, bis(triphenylphosphine)palladium(II) dichloride ($\text{Pd}(\text{PPh}_3)_2\text{Cl}_2$), KOH, 40% NaOH solution, tetra-*n*-butylammonium hydrogen sulfate (TBAHS), tetra-*n*-butylammonium bromide (TBABr), potassium carbonate (K_2CO_3), phosphorus trichloride (POCl_3) and dimethylformamide (DMF) were purchased from Aldrich and used as received. 10-Hexylphenoxazine (3) and 10-hexylphenothiazine (4) were prepared from 10*H*-phenoxazine (1) or 10*H*-phenothiazine (2) by alkylation reaction with 1-bromohexane according to the procedure outlined in the literature.⁶³ 3-Formyl-10-hexylphenoxazine (5) and 3-formyl-10-hexylphenothiazine (6) were obtained by Vilsmeier-Haack formylation reaction of the 10-hexylphenoxazine (3) or 10-hexylphenothiazine (4) according to the described procedure.⁶⁴ 10-Hexyl-3-(2,7-dibromofluoren-9-ylmethylene)phenoxazine (7) was prepared by the reaction of 3-formyl-10-hexylphenoxazine (5) with an excess of 2,7-dibromofluorene. The aldehyde 5 (1.0 g, 3.39 mmol) and 2,7-dibromofluorene (1.3 g, 4.07 mmol) were dissolved in toluene (10 ml) at 100 °C. Then 0.55 g (1.71 mmol) of TBABr and 40% NaOH (10 ml) were added into the solution. The resulting mixture was stirred at 100 °C for 10 min. At the end, the reaction mixture was quenched with ice water and extracted with chloroform. The organic solvent was evaporated using a rota-evaporator and the crude solid was purified by silica gel column chromatography using a mixture of tetrahydrofuran and hexane (vol. ratio 1 : 100) as an eluent. Yield: 1.3 g (64%) of red amorphous product. MS (APCI +, 20 V): 603.28 ($[\text{M} + \text{H}]$, 100%). ¹H NMR (400 MHz, DMSO, δ): 8.17 (s, 1H, CH), 7.98 (s,

1H, Ar), 7.93–7.80 (m, 3H, Ar), 7.62–7.51 (m, 2H, Ar), 7.15 (d, 1H, $J = 8.4 \text{ Hz}$, A), 6.95–6.67 (m, 6H, Ar), 3.63 (t, 2H, $J = 7.6 \text{ Hz}$, NCH_2), 1.67–1.53 (m, 2H, NCH_2CH_2), 1.48–1.38 (t, 2H, $\text{NCH}_2\text{CH}_2\text{CH}_2$), 1.38–1.27 (m, 4H, $\text{NCH}_2\text{CH}_2\text{CH}_2\text{CH}_2\text{CH}_2$), 0.88 (t, 3H, $J = 6.8 \text{ Hz}$, CH_3).

10-Hexyl-3-(2,7-dibromofluoren-9-ylmethylene)phenothiazine (8) was prepared by the reaction of 3-formyl-10-hexylphenothiazine (6) with an excess of 2,7-dibromofluorene. The aldehyde 6 (2.0 g, 6.43 mmol) and 2,7-dibromofluorene (2.5 g, 7.72 mmol) were dissolved in toluene (20 ml) at 100 °C. Then 1.04 g (3.23 mmol) of TBABr and 40% NaOH (10 ml) were added into the solution. The resulting mixture was stirred at 100 °C for 15 min. At the end, the reaction mixture was quenched with ice water and extracted with chloroform. The organic solvent was evaporated using a rota-evaporator and the crude solid was purified by silica gel column chromatography using a mixture of tetrahydrofuran and hexane (vol. ratio 1 : 100) as an eluent. Yield: 3.0 g (76%) of red amorphous product. MS (APCI +, 20 V): 616.02 ($[\text{M} + \text{H}]$, 100%). ¹H NMR (400 MHz, DMSO, δ): 8.14 (s, 1H, CH), 7.91 (s, 1H, Ar), 7.87–7.75 (m, 3H, Ar), 7.60–7.31 (m, 4H, Ar), 7.28–6.89 (m, 5H, Ar), 3.90 (t, 2H, $J = 6.8 \text{ Hz}$, NCH_2), 1.77–1.62 (m, 2H, NCH_2CH_2), 1.45–1.33 (m, 2H, $\text{NCH}_2\text{CH}_2\text{CH}_2$), 1.32–1.20 (m, 4H, $\text{NCH}_2\text{CH}_2\text{CH}_2\text{CH}_2\text{CH}_2$), 0.81 (t, 3H, $J = 6.8 \text{ Hz}$, CH_3).

10-Hexyl-3-[2,7-di(naphthalen-1-yl)fluoren-9-ylmethylene]phenoxazine (DNFPhe) (9). 0.3 g (0.5 mmol) of 10-hexyl-3-(2,7-dibromofluoren-9-ylmethylene)phenoxazine (7), 0.26 g (1.5 mmol) of naphthalene-1-boronic acid, 0.014 g (0.02 mmol) of $\text{PdCl}_2(\text{PPh}_3)_2$ and 0.14 g (2.5 mmol) of powdered KOH were stirred in 8 ml of THF containing degassed water (1 ml) at 80 °C under nitrogen for 1 h. After TLC control the reaction mixture was cooled and quenched by the addition of ice water. The product was extracted with chloroform. The combined extract was dried over anhydrous Na_2SO_4 . The crude product was purified by silica gel column chromatography using a mixture of tetrahydrofuran and hexane (vol. ratio 1 : 9) as an eluent. Yield: 0.3 g of red amorphous product (79%). MS (APCI+, 20 V): 781.07 ($[\text{M} + \text{Na}]$, 100%). ¹H NMR (400 MHz, DMSO, δ): 8.13–7.85 (m, 10H, CH, Ar), 7.80 (s, 1 H, Ar), 7.68–7.43 (m, 10H, Ar), 7.28–7.19 (m, 1H, Ar), 6.91 (s, 1H, Ar), 6.85–6.75 (m, 1H, Ar), 6.70–6.52 (m, 4H, Ar), 3.49 (t, 2H, $J = 8.4 \text{ Hz}$, NCH_2), 1.39–1.25 (m, 4H, $\text{NCH}_2\text{CH}_2\text{CH}_2$), 1.25–1.16 (m, 4H, $\text{NCH}_2\text{CH}_2\text{CH}_2\text{CH}_2\text{CH}_2$), 0.84 (t, 3H, $J = 6.8 \text{ Hz}$, CH_3). ¹³C NMR (400 MHz, CDCl_3 , δ): 149.03, 148.93, 146.47, 145.05, 144.72, 144.61, 144.31, 143.65, 141.40, 138.83, 138.88, 138.39, 137.20, 136.33, 136.28, 135.86, 133.48, 132.18, 131.82, 131.19, 130.72, 128.95, 126.46, 123.78, 120.93, 120.44, 117.38, 116.79, 36.20, 26.34, 25.96, 27.36, 19.11. FT-IR (KBr), cm^{-1} : 3045, 2924, 2852, 2620, 2080, 1982, 1813, 1742, 1623, 1587, 1489, 1415, 1381, 1272, 1132, 1080, 1045, 938, 862, 799, 775, 736.

10-Hexyl-3-[2,7-di(4-(diphenylamino)phenyl)fluoren-9-ylmethylene]phenoxazine (DDPPFPhe) (10). 0.3 g (0.5 mmol) of 10-hexyl-3-(2,7-dibromofluoren-9-ylmethylene)phenoxazine (7), 0.43 g (1.5 mmol) of naphthalene-1-boronic acid, 0.014 g (0.02 mmol) of $\text{PdCl}_2(\text{PPh}_3)_2$ and 0.14 g (2.5 mmol) of powdered KOH were stirred in 10 ml of THF containing degassed water (1 ml) at 80 °C under nitrogen for 1 h. After TLC control the reaction mixture was cooled

and quenched by the addition of ice water. The product was extracted with chloroform. The combined extract was dried over anhydrous Na_2SO_4 . The crude product was purified by silica gel column chromatography using a mixture of tetrahydrofuran and hexane (vol. ratio 1:20) as an eluent. Yield: 0.4 g of yellow crystals (85%). M.p.: 184 °C (DSC). MS (APCI⁺, 20 V): 930.43 ([M + H], 100%). ¹H NMR (400 MHz, DMSO, δ): 8.23 (s, 1H, CH), 8.11 (s, 1H, Ar), 8.01–7.85 (m, 3H, Ar), 7.80–7.45 (m, 6H, Ar), 7.43–7.17 (m, 9H, Ar), 7.16–6.75 (m, 19H, Ar), 6.73–6.48 (m, 3H, Ar), 3.60 (t, 2H, $J = 7.2$ Hz, NCH_2), 1.56–1.43 (m, 2H, NCH_2CH_2), 1.40–1.31 (m, 2H, $\text{NCH}_2\text{CH}_2\text{CH}_2$), 1.28–1.2 (m, 4H, $\text{NCH}_2\text{CH}_2\text{CH}_2\text{CH}_2\text{CH}_2$), 0.83 (t, 3H, $J = 6.8$ Hz, CH_3). ¹³C NMR (400 MHz, CDCl_3 , δ): 147.55, 147.39, 134.95, 130.09, 130.05, 127.90, 124.68, 124.57, 124.53, 122.72, 122.82, 119.99, 119.05, 31.55, 22.61, 21.34, 14.39. FT-IR (KBr), cm^{-1} : 3045, 2952, 2924, 2853, 2324, 2116, 1996, 1812, 1623, 1587, 1489, 1462, 1380, 1271, 1186, 1132, 1080, 1043, 888, 824, 799, 775, 737.

10-Hexyl-3-[2,7-di(4-fluorophenyl)fluoren-9-ylmethylene]phenoxazine (DFPFPh) (11). 0.3 g (0.5 mmol) of 10-hexyl-3-(2,7-dibromofluoren-9-ylmethylene)phenoxazine (7), 0.21 g (1.5 mmol) of 4-fluorophenylboronic acid, 0.014 g (0.02 mmol) of $\text{PdCl}_2(\text{PPh}_3)_2$ and 0.14 g (2.5 mmol) of powdered KOH were stirred in 10 ml of THF containing degassed water (1 ml) at 80 °C under nitrogen for 1 h. After TLC control the reaction mixture was cooled and quenched by the addition of ice water. The product was extracted with chloroform. The combined extract was dried over anhydrous Na_2SO_4 . The crude product was purified by silica gel column chromatography using a mixture of tetrahydrofuran and hexane (vol. ratio 1:20) as an eluent. Yield: 0.25 g of yellow crystals (79%). M.p.: 158 °C (DSC). MS (APCI⁺, 20 V): 632.52 ([M + H], 100%). ¹H NMR (400 MHz, DMSO, δ): 8.25 (s, 1H, CH), 8.14 (s, 1H, Ar), 8.01–7.81 (m, 5H, Ar), 7.73–7.55 (m, 4H, Ar), 7.40–7.09 (m, 5H, Ar), 7.04 (s, 1H, Ar), 6.97–6.71 (m, 5H, Ar), 3.63 (t, 2H, $J = 6.8$ Hz, NCH_2), 1.61–1.52 (m, 2H, NCH_2CH_2), 1.47–1.38 (m, 2H, $\text{NCH}_2\text{CH}_2\text{CH}_2$), 1.36–1.24 (m, 4H, $\text{NCH}_2\text{CH}_2\text{CH}_2\text{CH}_2\text{CH}_2$), 0.87 (t, 3H, $J = 6.8$ Hz, CH_3). ¹³C NMR (400 MHz, DMSO, δ): 144.56, 144.28, 140.83, 138.65, 137.38, 134.28, 134.04, 132.71, 129.22, 129.14, 128.90, 128.82, 128.76, 127.44, 126.75, 124.82, 121.86, 120.90, 116.03, 115.68, 112.86, 31.60, 26.22, 24.80, 22.61, 14.34. FT-IR (KBr), cm^{-1} : 3062, 2956, 2925, 2854, 2324, 2081, 1983, 1888, 1760, 1623, 1587, 1513, 1490, 1461, 1382, 1273, 1229, 1157, 1139, 1043, 1013, 890, 840, 803, 778, 741.

10-Hexyl-3-(2,7-diphenylfluoren-9-ylmethylene)phenoxazine (DPPPh) (12). 0.3 g (0.5 mmol) of 10-hexyl-3-(2,7-dibromofluoren-9-ylmethylene)phenoxazine (7), 0.5 g (1.5 mmol) of phenylboronic acid, 0.014 g (0.02 mmol) of $\text{PdCl}_2(\text{PPh}_3)_2$ and 0.14 g (2.5 mmol) of powdered KOH were stirred in 8 ml of THF containing degassed water (1 ml) at 80 °C under nitrogen for 1 h. After TLC control the reaction mixture was cooled and quenched by the addition of ice water. The product was extracted with chloroform. The combined extract was dried over anhydrous Na_2SO_4 . The crude product was purified by silica gel column chromatography using a mixture of tetrahydrofuran and hexane (vol. ratio 1:50) as an eluent. Yield: 0.2 g of yellow crystals (68%). M.p.: 144 °C (DSC). MS (APCI⁺, 20 V): 596.57 ([M + H], 100%). ¹H NMR (400 MHz,

DMSO, δ): 8.28 (s, 1H, CH), 8.20 (s, 1H, Ar), 8.05–7.92 (m, 3H, Ar), 7.88–7.79 (m, 2H, Ar), 7.77–7.47 (m, 6H, Ar), 7.45–7.22 (m, 5H, Ar), 7.08 (m, 1H, Ar), 6.97–6.70 (m, 5H, Ar), 3.65 (t, 2H, $J = 7.6$ Hz, NCH_2), 1.64–1.57 (m, 2H, NCH_2CH_2), 1.49–1.40 (m, 2H, $\text{NCH}_2\text{CH}_2\text{CH}_2$), 1.38–1.26 (m, 4H, $\text{NCH}_2\text{CH}_2\text{CH}_2\text{CH}_2\text{CH}_2$), 0.88 (t, 3H, $J = 6.8$ Hz, CH_3). ¹³C NMR (400 MHz, DMSO, δ): 145.38, 144.76, 140.68, 139.95, 139.14, 137.36, 134.94, 130.68, 129.70, 129.39, 128.33, 127.78, 127.24, 126.85, 123.84, 123.41, 1.26, 120.98, 116.51, 116.20, 47.09, 31.27, 26.56, 26.25, 22.52, 14.28. FT-IR (KBr), cm^{-1} : 3072, 3060, 2953, 2924, 2853, 2622, 2224, 2116, 1983, 1888, 1742, 1652, 1588, 1515, 1492, 1460, 1415, 1382, 1280, 1230, 1134, 1043, 1028, 998, 882, 862, 821, 759, 738.

10-Hexyl-3-[2,7-di(naphthalen-1-yl)fluoren-9-ylmethylene]phenothiazine (DNFPh) (13). 0.3 g (0.5 mmol) of 10-hexyl-3-(2,7-dibromofluoren-9-ylmethylene)phenothiazine (8), 0.25 g (1.5 mmol) of naphthalene-1-boronic acid, 0.014 g (0.02 mmol) of $\text{PdCl}_2(\text{PPh}_3)_2$ and 0.14 g (2.5 mmol) of powdered KOH were stirred in 8 ml of THF containing degassed water (1 ml) at 80 °C under nitrogen for 1 h. After TLC control the reaction mixture was cooled and quenched by the addition of ice water. The product was extracted with chloroform. The combined extract was dried over anhydrous Na_2SO_4 . The crude product was purified by silica gel column chromatography using a mixture of tetrahydrofuran and hexane (vol. ratio 1:50) as an eluent. Yield: 0.32 g of yellow amorphous material (92%). MS (APCI⁺, 20 V): 712.55 ([M + H], 100%). ¹H NMR (400 MHz, DMSO, δ): 8.17–7.84 (m, 11H, CH, Ar), 8.70–7.35 (m, 12H, Ar), 7.24–7.04 (m, 2H, Ar), 7.01–6.86 (m, 3H, Ar), 3.73 (t, 2H, $J = 6.4$ Hz, NCH_2), 1.52–1.41 (m, 2H, NCH_2CH_2), 1.31–1.16 (t, 2H, $\text{NCH}_2\text{CH}_2\text{CH}_2$), 1.15–0.96 (m, 4H, $\text{NCH}_2\text{CH}_2\text{CH}_2\text{CH}_2\text{CH}_2$), 0.72 (t, 3H, $J = 7.2$ Hz, CH_3). ¹³C NMR (400 MHz, DMSO, δ): 145.07, 144.52, 140.28, 140.24, 139.97, 139.88, 137.54, 134.67, 134.01, 131.09, 130.45, 130.36, 129.77, 128.84, 128.14, 127.61, 127.43, 127.09, 126.44, 126.05, 125.73, 123.94, 123.24, 123.13, 120.91, 116.34, 47.09, 31.12, 26.34, 26.08, 22.41, 14.19. FT-IR (KBr), cm^{-1} : 3055, 2952, 2924, 2853, 2324, 2115, 1995, 1733, 1626, 1592, 1574, 1493, 1461, 1415, 1384, 1275, 1174, 1076, 892, 820, 748, 730.

10-Hexyl-3-[2,7-di(4-(diphenylamino)phenyl)fluoren-9-ylmethylene]phenothiazine (DDPPPh) (14). 0.3 g (0.5 mmol) of 10-hexyl-3-(2,7-dibromofluoren-9-ylmethylene)phenothiazine (8), 0.42 g (1.5 mmol) of 4-(diphenylamino)phenylboronic acid, 0.014 g (0.02 mmol) of $\text{PdCl}_2(\text{PPh}_3)_2$ and 0.14 g (2.5 mmol) of powdered KOH were stirred in 10 ml of THF containing degassed water (1 ml) at 80 °C under nitrogen for 1 h. After TLC control the reaction mixture was cooled and quenched by the addition of ice water. The product was extracted with chloroform. The combined extract was dried over anhydrous Na_2SO_4 . The crude product was purified by silica gel column chromatography using a mixture of tetrahydrofuran and hexane (vol. ratio 1:20) as an eluent. Yield: 0.3 g of yellow crystals (65%). M.p.: 231 °C (DSC). MS (APCI⁺, 20 V): 946.53 ([M + H], 100%). ¹H NMR (400 MHz, CDCl_3 , δ): 7.97 (s, 1H, CH), 7.87 (s, 1H, Ar), 7.72–7.38 (m, 8H, Ar), 7.35–7.04 (m, 18H, Ar), 7.03–6.92 (m, 9H, Ar), 6.91–6.65 (m, 5H, Ar), 3.85 (t, 2H, $J = 6.8$ Hz, NCH_2), 1.81–1.65 (m, 2H, NCH_2CH_2), 1.40–1.27 (m, 2H, $\text{NCH}_2\text{CH}_2\text{CH}_2$), 1.25–1.18 (m, 4H, $\text{NCH}_2\text{CH}_2\text{CH}_2\text{CH}_2\text{CH}_2$), 0.77 (t, 3H, $J = 7.2$ Hz, CH_3). ¹³C NMR (400 MHz, CDCl_3 , δ): 147.80,

147.20, 134.85, 129.37, 129.30, 129.25, 127.80, 127.40, 124.40, 124.06, 123.98, 122.92, 122.82, 119.99, 119.86, 31.40, 26.63, 22.60, 14.01. FT-IR (KBr), cm^{-1} : 3061, 3031, 2953, 2925, 2854, 2325, 2115, 1996, 1790, 1731, 1627, 1588, 1512, 1491, 1462, 1411, 1384, 1315, 1275, 1173, 1134, 1076, 1028, 892, 820, 748, 730.

4.2. Materials and characterizations

In this research work, we have utilised pre-patterned indium tin oxide (ITO) glass substrates having a sheet resistance of $15 \Omega \square^{-1}$, which were purchased from Shine Materials Technology, Co. Ltd, Taiwan. The aqueous solution of bifunctional material, *i.e.* poly(3,4-ethylene-dioxythiophene)-poly-(styrene sulfonate) (PEDOT:PSS) (UR-AI4083), was bought from Uni-region Biotech, Taiwan. The phenothiazine and phenoxazine substituted fluorene cored novel hole-transport materials, *i.e.* **DNFPhe**, **DDPPFhe**, **DFFPFhe**, **DPFPhe**, **DDPPFPhe**, and **DNFPhe**, were synthesized in our laboratory. The primary materials, *i.e.* 10*H*-phenoxazine (**1**), 10*H*-phenothiazine (**2**), 1-bromohexane, 2,7-dibromofluorene, naphthalene-1-boronic acid, 4-(diphenylamino)phenylboronic acid, 4-fluorophenylboronic acid, phenylboronic acid, bis(triphenylphosphine)palladium(II) dichloride ($\text{Pd}(\text{PPh}_3)_2\text{Cl}_2$), KOH, 40% NaOH solution, tetra-*n*-butylammonium hydrogen sulfate (TBAHS), tetra-*n*-butylammonium bromide (TBABr), potassium carbonate (K_2CO_3), phosphorus trichloride (POCl_3) and dimethylformamide (DMF), were bought from Aldrich and used as received for the synthesis of these novel materials. The organic materials utilised in this research work, *i.e.* 4,4'-Bis(*N*-carbazolyl)-1,1'-biphenyl (CBP) as a host, iridium(III)bis(4-phenylthieno[3,2-*c*]pyridinato-*N,C2'*) acetylacetonate (**PO-01**) as a phosphorescent yellow emitter, 2,4,5,6-tetra(9*H*-carbazol-9-yl)isophthalonitrile (**4CzIPN**) as a TADF green emitter, 1,3,5-tris(*N*-phenylbenzimidazol-2-yl)benzene (TPBi) as an electron-transport material, and lithium fluoride (LiF) as an electron-injection material, were bought from Shine Materials Technology Co. Ltd, Taiwan. Moreover, aluminium ingots (Al) were incorporated as the cathode material, which was purchased from Show Chemicals, Japan.

Bruker Avance III (400 MHz) apparatus was used for recording ^1H and ^{13}C nuclear magnetic resonance (NMR) spectra. The data are provided as chemical shifts (δ) in ppm against trimethylsilane. A Waters ZQ 2000 mass spectrometer was utilized for recording the mass spectra.

The thermal properties of these novel materials were established with Thermo-gravimetric analysis (TGA) and differential scanning calorimetry (DSC) on a TGAQ50 apparatus and Bruker Reflex II thermos-system, respectively. The TGA and DSC curves were measured in a nitrogen atmosphere at a heating rate of $10 \text{ }^\circ\text{C min}^{-1}$. The photophysical properties, *i.e.* ultraviolet-visible (UV-vis) spectrum, photoluminescence (PL) spectra at room temperature, and photoluminescence (PL) spectra at 77 K, of these materials dissolved as 1 mg ml^{-1} concentration into solvent, were observed with a Shimadzu UV-2450, Perkin Elmer LS55 and Hitachi F-7000 fluorescence spectrophotometer with a delay time of 6.31 ms instruments, respectively. The UV-vis spectra edge wavelength was used to measure the

optical bandgap energy. The excitation wavelength and scan rates were 350 nm and $10 \text{ nm minute}^{-1}$, respectively, during the PL spectra measurement at room temperature. The triplet energy has been determined from the phosphorescence spectra. The surface morphology was measured by atomic force microscopy using a Bruker's scanning probe microscope. The samples for the AFM measurement were prepared by spin-coating HTMs on PEDOT:PSS deposited ITO substrates. The electrochemical analysis of these novel materials was carried out with a cyclic voltammetry (CV) set-up mounted with a computer. The electrochemical system consisted of three electrodes including a glassy carbon electrode as a working point, a platinum rod as an auxiliary electrode, and a silver/silver chloride rod as the reference electrode. The electrochemical analysis was carried out with a CH-instruments CH1604A potentiostat at room temperature under a nitrogen environment in dichloromethane (DCM) using 0.1 M tetrabutylammonium perchlorate (Bu_4NClO_4) as the auxiliary electrolyte material.

4.3. Device fabrication and characterizations

The schematic energy-level diagram of studied phosphorescent and TADF OLED devices is shown in Fig. 6. These devices were fabricated with the following device configurations: ITO (125 nm)/PEDOT:PSS (35 nm)/HTMs/CBP:12.5 wt% **PO-01** (20 nm)/TPBi (40 nm)/LiF (1 nm)/Al (200 nm) and ITO (125 nm)/PEDOT:PSS (35 nm)/HTMs/CBP:5 wt% **4CzIPN** (20 nm)/TPBi (40 nm)/LiF (1 nm)/Al (200 nm).

Initially, for the phosphorescent yellow OLED, the aqueous solution of PEDOT:PSS was spin-coated at 4000 rpm for 20 s to deposit as a hole-injection layer on a precleaned ITO anode, which was sputtered on the glass substrates. Then, the prepared substrates were kept on a hot plate for heating PEDOT:PSS thin-film for 30 min at $100 \text{ }^\circ\text{C}$. Then, the solution of newly synthesized HTMs was prepared by mixing 4 mg ml^{-1} in tetrahydrofuran at room temperature with stirring for 0.5 h before spin-coating. The resulting solution was then spin-coated at 2500 rpm for 20 s under nitrogen and the samples were kept on the hot plate at $60 \text{ }^\circ\text{C}$ for 30 min. After that, the premixed host-guest solution was spin-coated at 2700 rpm for 20 s and the resultant film was gradually annealed in a vacuum chamber. This was followed by the deposition of an electron-transporting layer TPBi, an electron-injection layer LiF, and a cathode Al, by thermal evaporation in a chamber with a vacuum level of 4×10^{-6} Torr.

For thermally activated delayed fluorescence green OLED, a solution of PEDOT:PSS was spin-coated on pre-cleaned ITO sputtered glass substrates to form a 35 nm thin film and kept on the hot plate at $100 \text{ }^\circ\text{C}$ for 30 min. Subsequently, the solution of newly synthesized HTMs was spin-coated on the PEDOT:PSS coated substrates and annealed on a hot plate for 30 min at $100 \text{ }^\circ\text{C}$. Afterwards, a 20 nm emissive layer (5 wt% **4CzIPN** doped in the CBP host) was deposited on the annealed HTMs *via* the solution process and the resultant film was annealed in a vacuum. Subsequently, a 40 nm electron-transport layer of TPBi, a 1 nm electron-injection

layer of LiF, and a 100 nm cathode Al were deposited using the thermal evaporation process.

After device fabrication, these devices were kept in a small vacuum chamber and used one by one for testing. The current–voltage–luminance (J – V – L) characteristics were measured with a computer mounted electrometer, *i.e.* a Keithley source measurement unit (CS-2400). After that, the Photo Research PR-655 spectrum scan and CS100A luminance meter were utilised to measure CIE chromatic coordinates, EL spectra, and luminance. The brightness of all the devices was measured in forward directions. Moreover, the device measurements were obtained in an artificial dark room.

To estimate the performance of OLED devices, external quantum efficiency (EQE) is a key parameter and can be calculated using the following equation: $EQE = \Phi_{PL} \times \gamma \times \eta_{S/T} \times \eta_{out}$, where Φ_{PL} , γ , $\eta_{S/T}$, and η_{out} denote the photoluminescence quantum yield (PLQY) of the emitters, the balance of charge carriers in the emissive zone, radiative exciton utilization efficiency, and light outcoupling efficiency, respectively. γ is 100% for balanced carriers and η_{out} is 20% for planer devices fabricated with organic layers.

Conflicts of interest

There are no conflicts of research.

Acknowledgements

This research was supported by the Ministry of Science and Technology (109-2923-M-007-003-MY3), Taiwan and TLL project 108-2923-M-007-002-MY3. In addition, the OLED materials have been developed in conjunction with the project and supported under the S-LLT-19-2 funding from the Lithuanian Research Council and the Taiwan MOST.

References

- 1 S. Sudheendran Swayamprabha, D. K. Dubey, S. Shahnawaz, R. A. K. Yadav, M. R. Nagar, A. Sharma, F.-C. Tung and J.-H. Jou, *Adv. Sci.*, 2021, **8**, 2002254.
- 2 J. Song, K. Lee and T. Khanna, *Calif. Manage. Rev.*, 2016, **58**, 118–140.
- 3 G. Hong, X. Gan, C. Leonhardt, Z. Zhang, J. Seibert, J. M. Busch and S. Bräse, *Adv. Mater.*, 2021, **33**, 2005630.
- 4 iPhone 12 Pro and iPhone 12 Pro Max - Apple, <https://www.apple.com/iphone-12-pro/>, (accessed 31 August 2021).
- 5 OLED TVs: Ultra Slim & LG 4K OLED TVs | LG India, <https://www.lg.com/in/oled-tvs>, (accessed 31 August 2021).
- 6 L. Zeng, E. Sun, J. Huang, Z. Wang and S. Liu, *SID Int. Symp. Dig. Tech. Pap.*, 2021, **52**, 652–654.
- 7 J.-H. Jou, S. Kumar, A. Agrawal, T.-H. Li and S. Sahoo, *J. Mater. Chem. C*, 2015, **3**, 2974–3002.
- 8 K. R. Justin Thomas, A. Venkateswararao, V. Joseph, S. Kumar and J.-H. Jou, *Org. Electron.*, 2019, **64**, 266–273.
- 9 X.-D. Zhao, Y.-Q. Li, H.-Y. Xiang, Y.-B. Zhang, J.-D. Chen, L.-H. Xu and J.-X. Tang, *ACS Appl. Mater. Interfaces*, 2017, **9**, 2767–2775.
- 10 OLEDs: Display's Next Big Thing | Applied Materials, <https://www.appliedmaterials.com/nanochip/nanochip-fab-solutions/november-2020/oled-displays-next-big-thing>, (accessed 2 September 2021).
- 11 C.-C. Huang, S.-F. Wu and M.-K. Fung, *SID Int. Symp. Dig. Tech. Pap.*, 2019, **50**, 1767–1770.
- 12 B. Balaganesan, H.-L. Huang, K.-F. Chiang, P.-W. Hsu and B.-W. Xie, *SID Int. Symp. Dig. Tech. Pap.*, 2014, **45**, 1558–1560.
- 13 J.-H. Jou, C.-Y. Hsieh, J.-R. Tseng, S.-H. Peng, Y.-C. Jou, J. H. Hong, S.-M. Shen, M.-C. Tang, P.-C. Chen and C.-H. Lin, *Adv. Funct. Mater.*, 2013, **23**, 2750–2757.
- 14 C. May, in *2021 28th International Workshop on Active-Matrix Flatpanel Displays and Devices (AM-FPD)*, 2021, pp. 42–45.
- 15 D. K. Dubey, G. Krucaite, S. S. Swayamprabha, R. A. K. Yadav, D. Blazevecius, J. Tagare, S. Chavhan, T.-C. Hsueh, S. Vaidyanathan, S. Grigalevicius and J.-H. Jou, *Org. Electron.*, 2020, **79**, 105633.
- 16 L. Duan, L. Hou, T.-W. Lee, J. Qiao, D. Zhang, G. Dong, L. Wang and Y. Qiu, *J. Mater. Chem.*, 2010, **20**, 6392–6407.
- 17 M. R. Nagar, S. Shahnawaz, R. A. K. Yadav, J.-T. Lin and J.-H. Jou, *ACS Appl. Electron. Mater.*, 2020, **2**, 1545–1553.
- 18 T. Huang, W. Jiang and L. Duan, *J. Mater. Chem. C*, 2018, **6**, 5577–5596.
- 19 J.-H. Jou, S. Sahoo, D. K. Dubey, R. A. K. Yadav, S. S. Swayamprabha and S. D. Chavhan, *J. Mater. Chem. C*, 2018, **6**, 11492–11518.
- 20 N. B. Kotadiya, P. W. M. Blom and G.-J. A. H. Wetzelaer, *Nat. Photonics*, 2019, **13**, 765–769.
- 21 R. A. K. Yadav, D. K. Dubey, S.-Z. Chen, T.-W. Liang and J.-H. Jou, *Sci. Rep.*, 2020, **10**, 9915.
- 22 S. Jhulki and J. N. Moorthy, *J. Mater. Chem. C*, 2018, **6**, 8280–8325.
- 23 A. P. Kulkarni, C. J. Tonzola, A. Babel and S. A. Jenekhe, *Chem. Mater.*, 2004, **16**, 4556–4573.
- 24 D. Thakur, M. R. Nagar, A. Tomar, D. K. Dubey, S. Kumar, S. S. Swayamprabha, S. Banik, J.-H. Jou and S. Ghosh, *ACS Appl. Electron. Mater.*, 2021, **3**, 2317–2332.
- 25 M. R. Nagar, R. A. K. Yadav, D. K. Dubey and J.-H. Jou, *MRS Adv.*, 2019, **4**, 1801–1809.
- 26 S. Shahnawaz, S. Sudheendran Swayamprabha, M. R. Nagar, R. A. K. Yadav, S. Gull, D. K. Dubey and J.-H. Jou, *J. Mater. Chem. C*, 2019, **7**, 7144–7158.
- 27 Y. Shirota, *J. Mater. Chem.*, 2005, **15**, 75–93.
- 28 S.-O. Jeon, K. S. Yook, C. W. Joo, J. Y. Lee, K.-Y. Ko, J.-Y. Park and Y. G. Baek, *Appl. Phys. Lett.*, 2008, **93**, 63306.
- 29 J. Kwak, Y.-Y. Lyu, S. Noh, H. Lee, M. Park, B. Choi, K. Char and C. Lee, *Thin Solid Films*, 2012, **520**, 7157–7163.
- 30 X. Zhao, S. Wang, J. You, Y. Zhang and X. Li, *J. Mater. Chem. C*, 2015, **3**, 11377–11384.
- 31 P. M. Borsenberger, E. H. Magin and J. J. Fitzgerald, *J. Phys. Chem.*, 1993, **97**, 8250–8253.
- 32 Y. Shirota, T. Kobata and N. Noma, *Chem. Lett.*, 1989, 1145–1148.

- 33 Y. Shirota, K. Okumoto and H. Inada, *Synth. Met.*, 2000, **111–112**, 387–391.
- 34 M. Y. Wong and E. Zysman-Colman, *Adv. Mater.*, 2017, **29**, 1605444.
- 35 J.-H. Jou, T.-H. Li, S. Kumar, C.-C. An, A. Agrawal, S.-Z. Chen, P.-H. Fang, G. Krucaite, S. Grigalevicius, J. Grazulevicius and C.-F. Sung, *Org. Electron.*, 2015, **24**, 254–262.
- 36 Y. Kuwabara, H. Ogawa, H. Inada, N. Noma and Y. Shirota, *Adv. Mater.*, 1994, **6**, 677–679.
- 37 J. Zhu, W. Song, T. Zhang, Q. Dong, J. Huang, H. Zhou and J. Su, *Dyes Pigm.*, 2021, **186**, 108981.
- 38 H. Ha, Y. J. Shim, D. H. Lee, E. Y. Park, I.-H. Lee, S.-K. Yoon and M. C. Suh, *ACS Appl. Mater. Interfaces*, 2021, **13**, 21954–21963.
- 39 C. Murawski, C. Fuchs, S. Hofmann, K. Leo and M. C. Gather, *Appl. Phys. Lett.*, 2014, **105**, 113303.
- 40 J. W. Jo, J. W. Jung, E. H. Jung, H. Ahn, T. J. Shin and W. H. Jo, *Energy Environ. Sci.*, 2015, **8**, 2427–2434.
- 41 R. S. Begunov, A. A. Sokolov, I. V. Fedyanin, V. O. Sakulina and M. A. Syroeshkin, *Mendeleev Commun.*, 2019, **29**, 184–186.
- 42 H. Zhang, H. Yao, J. Hou, J. Zhu, J. Zhang, W. Li, R. Yu, B. Gao, S. Zhang and J. Hou, *Adv. Mater.*, 2018, **30**, 1800613.
- 43 Y. Zhang, S.-C. Chien, K.-S. Chen, H.-L. Yip, Y. Sun, J. A. Davies, F.-C. Chen and A. K.-Y. Jen, *Chem. Commun.*, 2011, **47**, 11026–11028.
- 44 J. R. Tumbleston, A. C. Stuart, E. Gann, W. You and H. Ade, *Adv. Funct. Mater.*, 2013, **23**, 3463–3470.
- 45 H. J. Son, W. Wang, T. Xu, Y. Liang, Y. Wu, G. Li and L. Yu, *J. Am. Chem. Soc.*, 2011, **133**, 1885–1894.
- 46 B. Carsten, J. M. Szarko, H. J. Son, W. Wang, L. Lu, F. He, B. S. Rolczynski, S. J. Lou, L. X. Chen and L. Yu, *J. Am. Chem. Soc.*, 2011, **133**, 20468–20475.
- 47 Z. Zhong, Y. Ma, H. Liu, F. Peng, L. Ying, S. Wang, X. Li, J. Peng and Y. Cao, *ACS Appl. Mater. Interfaces*, 2020, **12**, 20750–20756.
- 48 M. J. Frisch, G. W. Trucks, H. B. Schlegel, G. E. Scuseria, M. A. Robb, J. R. Cheeseman, G. Scalmani, V. Barone, B. Mennucci, G. A. Petersson, H. Nakatsuji, M. Caricato, X. Li, H. P. Hratchian, A. F. Izmaylov, J. Bloino, G. Zheng, J. L. Sonnenberg, M. Hada, M. Ehara, K. Toyota, R. Fukuda, J. Hasegawa, M. Ishida, T. Nakajima, Y. Honda, O. Kitao, H. Nakai, T. Vreven, J. A. Montgomery, J. E. Peralta, F. Ogliaro, M. Bearpark, J. J. Heyd, E. Brothers, K. N. Kudin, V. N. Staroverov, R. Kobayashi, J. Normand, K. Raghavachari, A. Rendell, J. C. Burant, S. S. Iyengar, J. Tomasi, M. Cossi, N. Rega, J. M. Millam, M. Klene, J. E. Knox, J. B. Cross, V. Bakken, C. Adamo, J. Jaramillo, R. Gomperts, R. E. Stratmann, O. Yazyev, A. J. Austin, R. Cammi, C. Pomelli, J. W. Ochterski, R. L. Martin, K. Morokuma, V. G. Zakrzewski, G. A. Voth, P. Salvador, J. J. Dannenberg, S. Dapprich, A. D. Daniels, Ö. Farkas, J. B. Foresman, J. V. Ortiz, J. Cioslowski and D. J. Fox, 2009.
- 49 M. Cossi, V. Barone, R. Cammi and J. Tomasi, *Chem. Phys. Lett.*, 1996, **255**, 327–335.
- 50 K. L. Woon, Z. A. Hasan, B. K. Ong, A. Ariffin, R. Griniene, S. Grigalevicius and S.-A. Chen, *RSC Adv.*, 2015, **5**, 59960–59969.
- 51 J.-H. Jou, S. Sahoo, S. Kumar, H.-H. Yu, P.-H. Fang, M. Singh, G. Krucaite, D. Volyniuk, J. V. Grazulevicius and S. Grigalevicius, *J. Mater. Chem. C*, 2015, **3**, 12297–12307.
- 52 Y. Deng, C. Keum, S. Hillebrandt, C. Murawski and M. C. Gather, *Adv. Opt. Mater.*, 2021, **9**, 2001642.
- 53 C. A. Amorim, M. R. Cavallari, G. Santos, F. J. Fonseca, A. M. Andrade and S. Mergulhão, *J. Non-Cryst. Solids*, 2012, **358**, 484–491.
- 54 T.-H. Han, W. Song and T.-W. Lee, *ACS Appl. Mater. Interfaces*, 2015, **7**, 3117–3125.
- 55 S. Il Lee, G. J. Yun, J. W. Kim, G. Hanta, K. Liang, L. Kojvic, L. S. Hui, A. Turak and W. Y. Kim, *Sci. Rep.*, 2019, **9**, 2411.
- 56 N. Liu, S. Mei, D. Sun, W. Shi, J. Feng, Y. Zhou, F. Mei, J. Xu, Y. Jiang and X. Cao, *Micromachines*, 2019, **10**, 344.
- 57 J. Lee, N. Chopra, S.-H. Eom, Y. Zheng, J. Xue, F. So and J. Shi, *Appl. Phys. Lett.*, 2008, **93**, 123306.
- 58 R.-Q. Png, P.-J. Chia, J.-C. Tang, B. Liu, S. Sivaramakrishnan, M. Zhou, S.-H. Khong, H. S. O. Chan, J. H. Burroughes, L.-L. Chua, R. H. Friend and P. K. H. Ho, *Nat. Mater.*, 2010, **9**, 152–158.
- 59 C.-H. Shih, P. Rajamalli, C.-A. Wu, M.-J. Chiu, L.-K. Chu and C.-H. Cheng, *J. Mater. Chem. C*, 2015, **3**, 1491–1496.
- 60 D. P.-K. Tsang, T. Matsushima and C. Adachi, *Sci. Rep.*, 2016, **6**, 22463.
- 61 S. Liu, C. Peng, A. Cruz, Y. Chen and F. So, *J. Mater. Chem. C*, 2016, **4**, 8696–8703.
- 62 Y. Tan, Z. Zhao, L. Shang, Y. Liu, C. Wei, J. Li, H. Wei, Z. Liu, Z. Bian and C. Huang, *J. Mater. Chem. C*, 2017, **5**, 11901–11909.
- 63 H. Tan, C. Pan, G. Wang, Y. Wu, Y. Zhang, Y. Zou, G. Yu and M. Zhang, *Org. Electron.*, 2013, **14**, 2795–2801.
- 64 M. Anil Reddy, B. Vinayak, T. Suresh, S. Niveditha, K. Bhanuprakash, S. Prakash Singh, A. Islam, L. Han and M. Chandrasekharam, *Synth. Met.*, 2014, **195**, 208–216.